UC Berkeley
UC Berkeley Electronic Theses and Dissertations

Title
Characterizing the Fatigue Behavior of the High-Entropy 'Cantor' Alloy CrCoMnFeNi

Permalink
https://escholarship.org/uc/item/7zb316wm

Author
Thurston, Keli Vieno Siukola

Publication Date
2018

Peer reviewed|Thesis/dissertation

Characterizing the Fatigue Behavior of the High-Entropy 'Cantor' Alloy CrCoMnFeNi

by

Keli Vieno Siukola Thurston

A dissertation submitted in partial satisfaction
of the requirements for the degree of
Doctor of Philosophy

in

Engineering – Materials Science and Engineering

in the

GRADUATE DIVISIONS
of the
UNIVERSITY OF CALIFORIA, BERKELEY

Committee in charge:
Professor Robert O. Ritchie, Chair
Professor Andrew Minor
Professor Lisa Pruitt

Fall 2018

Abstract

Characterizing the Fatigue Behavior of the High-Entropy "Cantor" Alloy CrCoMnFeNi

by

Keli Vieno Siukola Thurston

Doctor of Philosophy in Engineering – Materials Science and Engineering

University of California, Berkeley

Professor Robert O. Ritchie, Chair

High-entropy alloys (HEAs) have spurred great interested in the in the materials community in recent years, primarily due to the intriguing properties certain members have been shown to display and due to the novel approach to alloy design they represent. Of this family of multi-component alloy systems, the near-equiatomic five component "Cantor" alloy CrCoMnFeNi is of particular note due to the remarkable mechanical properties this alloy has been found to display which are only enhanced as the temperature is lowered into the cryogenic regime. Despite the interest in this alloy system, little work has to date been conducted that characterize the cyclic fatigue loading behavior of this alloy or of its compositional variants. Here I examine the damage-tolerant fatigue behavior of the Cantor alloy as well as the effect temperature and load ratio have in changing this behavior and the underlying mechanisms that may be responsible for the observed shifts. These testing conditions encompassed three temperature regimes: 293 K, 198 K, and 77 K; additionally, the impact of increased load ratio R was surveyed within each temperature regime. Fatigue testing in the threshold and linear portion of the Paris regime revealed a temperature dependence of the fatigue behavior of the Cantor alloy; as temperature was decreased into the cryogenic regime, the fatigue curve was found to shift toward higher ΔK, indicating a higher resistance to fatigue-crack propagation at lower temperature. Additionally, it was observed that higher load ratios impacted this resistance negatively, causing a shift towards lower ΔK with increasing R-ratio. Post-testing, a series of mechanistic studies were conducted to investigate the underlying cause for this observed shift. Analyses of crack closure measurements, crack-path morphology, and fractography provided strong evidence for roughness-induced crack closure as the dominant mechanism at play.

1

To those who are full of determination

(especially you, MLST)

Acknowledgements

This journey has been long and arduous but not one I have had to travel alone. Rather, many have contributed to make this project a successful one, more than I can detail fully. Whether through direct collaboration or indirect support, you have my deepest gratitude.

However, I would like spend these few words to recognize and thank some of you in greater detail. Chiefly, Professor Ritchie and my fellow group members. Professor Ritchie and Bernd, you two taught me so much and acted as wonderful mentors both within the laboratory space and without. My Ritchie group PhD cohort, you're the best. Whether it was giving me a break so I could go take a nap during a long dry-ice test, helping prep for the exams, or providing constructive feedback, I could always count on you. Perhaps we'll collaborate in the future; regardless, I've made several lasting friendships here.

Additionally, I would like the thank the many undergraduate and master's students who worked directly with me to get these tests up and running. Edwin, Jessica, and Julian, thank you so much for the work you put in; it really means a lot to me. Mingxi and Andrew, we may not have worked directly as much, but I've loved having you as colleagues as well, sharing ideas, stories, cookies.

Next, moving away from the laboratory space, I must acknowledge my other graduate school colleagues and friends. While our work may differ widely (from other MSE subfields to environmental biology to economics/finance to pottery), our successes and stumbles along the path to the degree are similar. You fellow travelers were wonderful companions, cheering me during the high points, supporting me during the low, and ensuring I took some time every so often to enjoy the vistas along the way.

Kiitos paljon, my family; I can't express how important you all are to me in a paltry couple of sentences. Leila and Brian, my mom and dad, you shaped me to be the person I am today, particularly evident in my love of books, crafting, and science. Matti, you've always being there for me; I couldn't ask for a better brother. Grandma Bev and Grandpa Phil, you've always supported me wholeheartedly in all my endeavors and continue to inspire me to this day. You all mean the world to me, and I'm so happy to have you all in my life!

Table of Contents

List of Figures

List of Tables

Chapter 1
Introduction

Our society's continual progress and growth drives a persistent demand for novel materials to fulfill roles and applications previously only dreamed of, step by step removing the 'fiction' from science. Metallic alloys continue to play a fundamental role in the basis of many of these technologies. As such, advancements in metallurgy and alloy design remain key steps on this path of scientific and engineering advancement. One of the most exciting subfields of metallurgical to emerge over the last decade or so has been the study of the "high entropy" alloy (HEA) family. This subfield has enjoyed enormous growth over the last few years, with each year seeing hundreds of more papers being published ranging from new members to the HEA family to characterizing their properties to proving their feasibility in practical applications.

This interest is well-founded as HEAs represent a major shift in approach to alloy design, one of humanities oldest technologies. Where conventional alloys consist of one or two majority elements, HEAs consist of five or more, often in near-equiatomic compositions, leading to a far greater number of potential alloy compositions and, in turn, vast potential for hitherto unseen material properties and behaviors. Properties of interest are as varied as the potential applications of metallic alloys, including but not limited to electrical, thermal, and mechanical; in this work, I will be focusing on the mechanical behavior of one particular HEA, specifically the fatigue behavior of the Cantor alloy.

While the Cantor alloy CrMnFeCoNi is attributed as the first described HEA and thus oldest member of this family of metals, it nevertheless remains one of the most promising in terms of its mechanical and structural properties, exhibiting excellent strength and toughness that only improves as the temperature is lowered into the cryogenic regime, disobeying the typical strength-toughness trade-off displayed by most metals at low temperature. However, as well-documented as many of this alloys properties have been, little work has been done to characterize the behavior of this alloy or any of its compositional variants under cyclic loading conditions, vital information to know before this alloy may be put into practical use; here I seek to bridge this gap.

Chapter 2
Background

High-entropy alloys (HEAs) represent a new approach to alloy design that has taken the metallurgical world by storm over the past few years as new metallic alloys have been found to exhibit unique combinations of properties; moreover, there is seemingly an unlimited number of potential new compositions that have yet to be explored. One particular HEA and its variants that have shown exceptional promise as structural materials is the so-called Cantor alloy, which is a single-phase, face-centered cubic solid-solution with an equiatomic CrMnFeCoNi composition. CrCoNi-based medium- and high-entropy alloys have been shown to have unprecedented combinations of strength, ductility and fracture toughness which are further improved at cryogenic temperatures; however, few studies have investigated their fatigue properties, either in terms of total stress/strain life or their crack propagation behavior. In general, these initial studies have indicated a relative similarity of the fatigue properties of the Cantor HEA variants with traditional steels of comparable strength and toughness. The precise energy dispersion mechanisms at play, however, remain contested and appear to differ with composition; current theories range from increased nano-scale twinning to crack closure effects although more studies are required to further explore the role of these phenomena. While some initial computer modeling studies have been conducted, the current lack of experimental fatigue studies on HEAs suggests a pressing need to verify and improve these models. More importantly, as fatigue is the most dominant failure mode for metallic structural materials, there is a more general need to mechanistically understand the cyclic deformation and fatigue failure properties of HEAs, both from a perspective of their potential use in practical applications and to help guide future alloy design.

2.1. GROWING INTEREST IN HIGH-ENTROPY ALLOYS

In the continuing quest for new and superior structural materials, high-entropy alloys (HEAs) present a fascinating proposition. First developed in the early 2000's by Cantor *et al.* [1] and Yeh *et al.* [2], HEAs represent an unbounded set of new metallic alloys, encompassing, in principle, stable (or meta-stable) solid solutions of at least five major constituent elements in nominal equiatomic concentrations. This is in stark contrast to traditional metallic alloys which comprise one (or two) dominant elements, such as iron in steels or nickel in superalloys, with small percentages of additional elements. The unusually high number of constituent elements has suggested to many the possibility of unusual mechanisms, such as local chemical ordering, sluggish diffusion, in situ phase transformation, and so forth; indeed, the fact that most of these potential new alloys have

never been made, analyzed or even contemplated previously has raised the additional possibility of finding materials with unprecedented combinations of mechanical and functional properties [3]. As society and technology advances, the constituent materials for these technologies must advance alongside them. This is especially true for structural materials, which are used primarily for their mechanical properties such as strength, toughness, and hardness. Structural materials are used everywhere: from the steel and concrete that comprises much of our infrastructure, to the composites and aluminum that our airframes are built from. Within this class of materials, metals have long dominated due to an excellent combination of factors. They tend to have excellent mechanical properties in terms of strength and toughness as well as exhibiting plasticity instead of catastrophic failure that increases their factor of safety and reliability in applications where extended use is needed. Furthermore, they are easily available with a wide range of tunable properties because of their ability to alloy with other metals and heat treatment cycles to maximize mechanical performance. Combining this all with their ability to be formed and machined in a variety of complex shapes makes them a difficult candidate to contend with for future materials.

The name "high-entropy alloy" originates from the early hypothesis that the high configurational entropy of these multi-element solutions would overwhelm the enthalpy of phase formation and thus be the key to permitting their stabilization into stable single-phase materials [4,5]. However, more recent studies, such as those conducted by Otto et al., indicate that the degree of configurational entropy exhibited by a solution is not the sole criteria; mixtures displaying high configurational entropies do not always form stable single-phase solid solutions [4]. Several studies have postulated that microstructural stability is primarily affected by entropic stabilization effects [5]. As such, the phrases used to describe this class of alloys have expanded to include 'multi-principal elements' or 'complex concentrated alloys'; however, the term 'high-entropy alloys' still prevails as most enduring within the materials communities and is expected to the one cemented into the metallurgical lexicon [5]. **Figure 2.1** exhibits the breath of solid solutions compositions that have come to be defined included in the category 'high-entropy alloys' with more members continually being added as new compositions are discovered and the definition broadens further; for example, some four-component alloy systems have been described as HEAs while others, such as three-component systems, have been classified as 'medium-entropy alloys' [7].

Figure 2.1: Overview of recently examined HEAs. The grouping into the above categories is based on the compositional similarity of the included HEAs [6].

While HEAs remained little more than a processing curiosity in the decade following their discovery, these alloy systems have gained significantly more attention over the past few years as initial investigations into the mechanical properties of the then most prominent HEA, the *equiatomic CrMnFeCoNi* 'Cantor alloy', yielded exceptional results. Early monotonic testing of this particular composition revealed high tensile strengths up to 1.28 GPa combined with high ductility (~60-70%) and fracture toughness values over 200 MPa√m [1,4,8,9]. Even more notable, the mechanical behavior of the Cantor alloy was found, at decreasing temperatures below ambient, not to degrade but rather to further improve without exhibiting the typical strength-ductility tradeoff observed in most metallic materials [10,11]. This trend continues well into the cryogenic temperature regime, with the Cantor alloy demonstrating mechanical behavior comparable, and, in some cases, exceeding the properties of state-of-the-art cryogenic steels [9,12].

Motivated by the exceptional mechanical properties of the Cantor alloy, there has been a significant resurgence in research to characterize other promising and prominent HEAs. Recent studies, for example, with an aluminum variant of the Cantor alloy, AlCrFeCoNi, found it to display yield and fracture strengths of 1450 MPa and 2960 MPa, respectively [13], values which with further modification with titanium-enrichment were

increased to 2.26 GPa and 3.14 GPa [14]. Other studies have led to new HEAs that demonstrate high hardness, high compressive yield strength, and outstanding wear resistance comparable to ferrous alloys with similar hardness that outperform SUJ2 wear-resistant steels [2,15-21]. More exotic compositions, such as NbSiTaTiZr, have been found to display thermal stability with excellent recrystallization behavior coupled with excellent oxidation and corrosion resistance [9,22,23]. With fifty or so usable elements in the periodic table, the number of new HEAs to be investigated, in terms of merely equiatomic five-component systems, runs into several tens of millions, and so probing this vast compositional space for new and useful alloys represents a major challenge, involving theoretical techniques, e.g., first-principles DFT or CALPHAD procedures, and/or machine learning algorithms, coupled with high-throughput experimental techniques (although the best ways to perform this daunting task remains unclear). However, despite the current feverish activities in the field of HEAs, one critical feature in terms of their mechanical performance remains under investigated, and that is failure under alternating loads - fatigue, despite its crucial role in the practical application of these engineering alloys.

The role of fatigue in mechanical failure first began to be appreciated in the mid-1880s with the failure of railroad axles; just under a hundred years later, the problem of fatigue came to even greater attention with the premature failures of the De Havilland Comets airliners, the first pressurized commercial jet aircraft, which resulted from fatigue cracks, growing in the aluminum alloy fuselage, that had initiated from the corners of the square windows. Now fatigue is recognized as a critical mode of fracture accounting for more than 80% of all in service failure involving accidents ranging from the mundane to the catastrophic [24,25]. Cyclic loading conditions can occur in many environments; as such, a proper understanding of a material's fatigue properties is vital in any engineering application that may touch on human lives. Proper characterization of subcritical crack-growth behavior can be used to construct accurate modern lifetime predictions of critical parts under predicted cyclic loading conditions, thus allowing both calculation of safety margins for a given material and a basis for comparison with other potential candidate materials, aiding and improving future design [26]. Further, fatigue calculations can determine the proper maintenance intervals for critical parts, allowing cost-saving longer intervals between preventative maintenance while ensuring operator and user safety [27,28].

Many of the catastrophic mechanical failures that have occurred can be traced to misunderstood or undiagnosed fatigue failure due to cyclic loading conditions over long intervals of subcritical loading. Yet despite the importance for understanding the fatigue behavior for materials that may be used in a structural capacity, few HEAs have been

investigated in this capacity either in terms of fatigue lifetime or in crack propagation behavior [29,30].

2.2. FATIGUE STUDIES OF HEAs

The studies of the fatigue properties of the HEA family as currently documented in the literature remain quite sparse. However, these examinations that have been conducted encompass a broad range of methods and techniques from total-life predictions to crack growth propagation rate analysis to computational modeling.

2.2.1. Total-life approach studies

The first published work that focused specifically on fatigue testing of HEAs was conducted by Hemphill *et al.* on a cast $Al_{0.5}CoCrCuFeNi$ alloy that displayed a two-phase face-centered cubic (fcc) structure with a major α-fcc phase and a copper-rich β-fcc phase [31]. The material was prepared by arc melting elements of ≥99% purity and annealing at 1000 °C for 6 h before being water quenched and cold rolled. Four-point bend specimens of size 25 x 3 x 3 mm were then constructed and tested in ambient conditions under cyclic loading at 10 Hz until failure or 10^{-7} cycles at an R-ratio, defined as the minimum divided by the maximum stress of the cyclic load conditions, of 0.1. The maximum stress levels varied between 540 – 1250 MPa with the upper boundary close to the examined yield stress of 1284 MPa. The related $Al_{7.5}Cr_{22.5}Fe_{35}Mn_{20}Ni_{15}$ alloy, a lower cost alternative, was later processed and tested under equivalent conditions [31,32].

The test results revealed a wide scatter over the tested stress levels with an endurance limit between 540 - 945 MPa for $Al_{0.5}CoCrCuFeNi$ and 540 - 630 MPa for the $Al_{7.5}Cr_{22.5}Fe_{35}Mn_{20}Ni_{15}$ alloy as listed in **Table 2.1**. The authors found no correlation between the occurred scatter and the orientation and morphology of the phases. Upon further investigation, they observed a trend related to the number of initial defects, particularly aluminum oxide-rich particles in the material; specimens that contained a lower number of defects in general performed better, with longer fatigue lifetimes [31]. The non-uniformity of defects within the entire sample set was hypothesized to be attributable to the casting process, allowing the increased introduction of phase segregation, inclusions, and microcracking in the material at sides of the casting which may then become exacerbated during the cold-rolling processes. Indeed, examination of the fracture surfaces showed that microcracks nucleated from the surface due to stress peaks introduced by the roughness and nucleated perpendicular to the load direction afterward. As the method of the weakest link suggests, the cracks initiated at the defects on the surface. Besides the high dependency of the fatigue life on initial defects, a linear

correlation between the ultimate tensile stress and the endurance limit was found with an approximate factor of 0.5; these results lend support for the theory that the high fatigue-limits of HEAs can be attributed to their high ultimate stress values [31].

Table 2.2: Overview of the total-life data regarding recently examined HEAs

Material	R-Ratio	Microstructure	Fatigue limit [Mpa]	Fatigue ratio
$Al_{0.5}CoCrCuFeNi$ [31,32]	0.1	as-cast	540-945	0.402-0.703
	0.1	as-cast (modified)	312-454	0.29
$Al_{7.5}Cr_{22.5}Fe_{35}Ni_{15}Mn$ [32]	0.1	as-cast	540-630	-
$Al_{0.1}CoCuFeNi$ [34]	-1	coarse-grained	200-210	0.36

The two-phase $Al_{0.5}CoCrCuFeNi$ was further investigated by Tang *et al*. [33]. To observe and quantify the impact of oxide inclusions and microcracks on the high scatter previously observed by Hemphill *et al*., three ingots were processed; two ingots were produced using commercial-purity elements (I + II) while the third was formed of high-purity elements (III). These ingots were repeatedly melted and solidified under vacuum to promote homogenization of the material before annealing and quenching under similar conditions previously conducted by Hemphill et al. Prior to the cold-rolling process, shrinkage pores and macro-segregations were removed from the surfaces of ingot II and III. Samples were machined, and testing conducted as previously described by Hemphill *et al. [*31].

The endurance limit of the S-N curve was found to be at 383 ±71 MPa and a fatigue limit to tensile strength ratio of 0.29; test results are shown in **Table 2.1**. Comparisons between the sample groups manufactured from the three ingots revealed that scatter in the results was significantly decreased through the use of high-purity elements and removal of macro-defects prior to testing as shown in **Figure 2.2**.
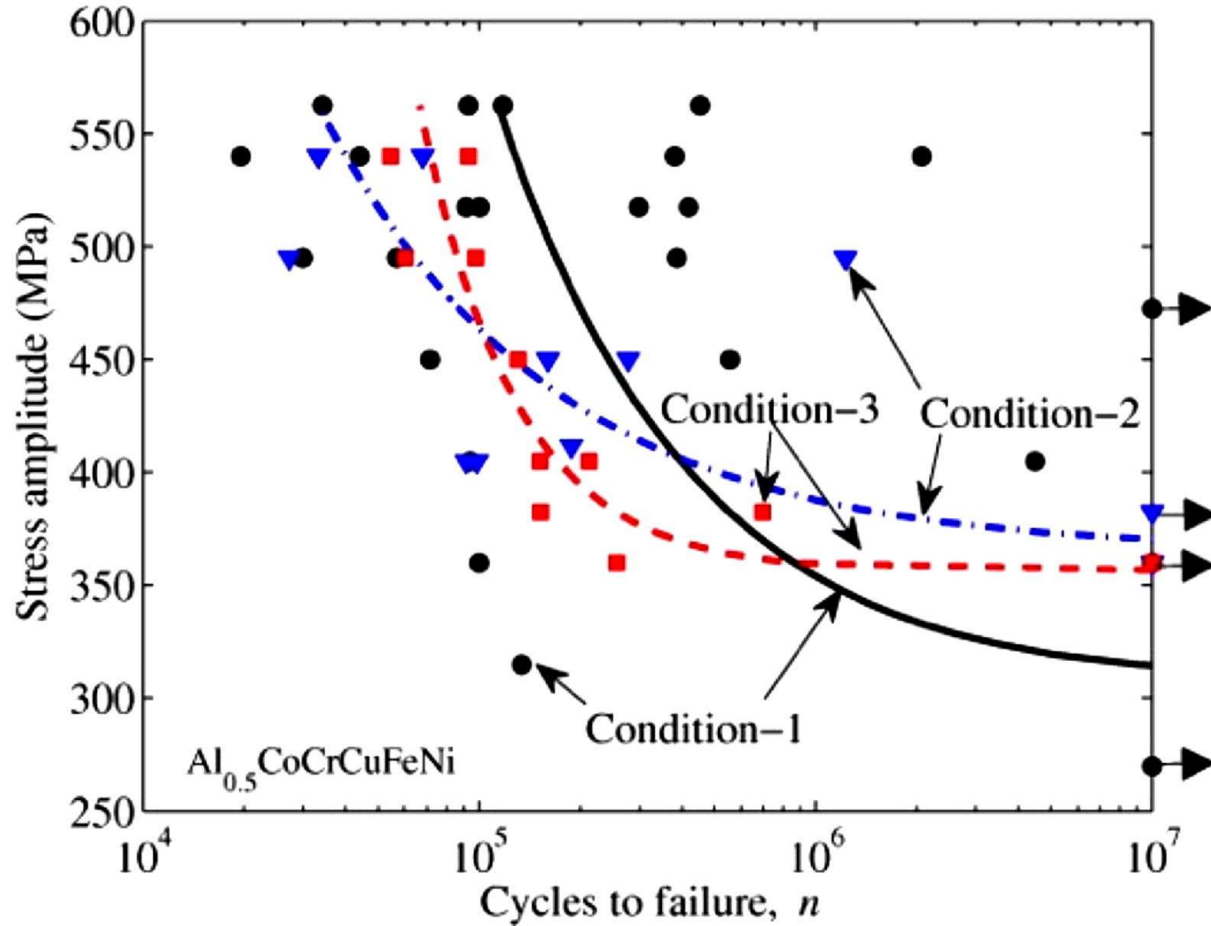
Figure 2.2: Stress range over cycles to failure for three separately processed $Al_{0.5}CoCrFeNi$ alloy systems at room temperature. The tests were performed with 10 Hz and an R-ratio of 0.1. Not failed specimens were marked with an arrow, indicating their probably higher lifetime. The lines show the results of the random endurance-limit fatigue model. Note the high scatter present in Condition 1 samples, similar to that which Hemphill observed. The endurance limit of the Condition 3 samples was found to be ~383 MPa [34].

Two additional copperless compositional variants of aluminum-containing HEA family have also recently been scrutinized for practical application in high-fatigue environments. The solid mechanical properties exhibited by $Al_{0.1}CoCrFeNi$ has caught the attention of the medical community and examined as a potential material for stents for cardiovascular applications [25]. The studies performed by Alagarsamy *et al.* differ from those by Hemphill *et al.* and Tang *et al.* in two critical ways beyond the compositional differences: here, the material was annealed at 1000 °C after the casting and cold-rolling process to eliminate the cast microstructure, and the testing R-ratio was -1 vs. 0.1. These differences make direct comparison difficult. Regardless, the coarse-grained $Al_{0.1}CoCrFeNi$ was found to demonstrate a solid endurance limit of 200-210 MPa with little scatter; in comparison, 316L stainless steel demonstrates similar mechanical

properties to CoCrFeNiMn, yet only exhibits an endurance limit of 184 MPa at a stress ratio of -1 [34].

A more recent study conducted by Liu *et al*. of $Al_{0.3}CoCrFeNi$ furthered the discussion of the relationship between the processing and fatigue properties of HEAs through examination of the role of grain size, specifically of an ultrafine-grained microstructure, and performance under fully reversible bending fatigue loading [35]. Implementing a method similar to Alagarsamy *et al*., the cast and solutionized samples were subjected to cold rolling to ~84% reduction and annealed at 700 $^{\circ}$C for 36 hr to achieve a three-phase material with the dominant FCC phase exhibiting an average grain size of 0.71 μm. As with Alagarsamy *et al*., samples were subjected to cyclic tension testing at an R-ratio of -1. Under these conditions, the fatigue runout of the HEA's S-N curve was found to be 450 MPa with a fatigue runout to tensile strength ratio of 0.43, the best performance yet reported for HEA systems tested in S-N fatigue [35]. As the composition remains similar, this data suggests the ultrafine grained microstructure plays a significant role in its superior performance.

In general, the total-life approach results generated by Hemphill *et al.* [31,32], Tang *et al*. [33], Alagarsamy *et al.* [25], and Liu *et al.* [35] indicate the aluminum-containing Cantor variants display favorable endurance limits comparable or superior to steels and other conventional alloys under the appropriate processing conditions, with much of the scatter and sensitivity in data collection linked to flaws potentially linked elemental purity and to the casting and/or cold-rolling conditions.

2.2.2. Crack Propagation studies

Seeking to characterize the fatigue crack propagation in HEAs, Seifi *et al*. investigated the impact of cyclic loading on the $Al_{0.2}CrFeNiTi_{0.2}$ and the $AlCrFeNi_2Cu$ alloy systems [36]. Both as-cast alloys were found to be multiphasic, dominated by two phases exhibiting face-centered cubic (fcc) and body-centered cubic (bcc) structures interwoven in a dendritic/interdendritic manner. To generate these samples, high purity elements were vacuum levitation melted and drop cast into a cylindrical mold before being machined into 3 x 5 x 47 mm bend bar samples. Samples were then subjected to cyclic testing at 20 Hz in ambient conditions with crack growth monitored using the direct current potential drop method. Additionally, Seifi *et al.* investigated the impact of load ratio during testing, performing tests at R-ratios = 0.1, 0.3, and 0.7. Results are summarized in **Table 2.2** and **Figure 2.3**.

Table 2.2: Test results produced by Seifi et al. for the $AlCrFeNi_2Cu$ and the $Al_{0.2}CrFeNiTi_{0.2}$ alloy for different R-ratios. Tests were performed with 20 Hz at room temperature [34].

Alloy	R (load ratio)	Fatigue overload K_c (MPa $\sqrt{m}$)	Paris slope (m)	Threshold (MPa $\sqrt{m}$)
AlCrFeNi$_2$Cu	0.1	56	3.4	17
AlCrFeNi$_2$Cu	0.3	36	6.5	5
AlCrFeNi$_2$Cu	0.7	32	14.5	7
Al$_{0.2}$CrFeNiTi$_{0.2}$	0.1	30	4.9	16
Al$_{0.2}$CrFeNiTi$_{0.2}$	0.3	23	5.3	7
Al$_{0.2}$CrFeNiTi$_{0.2}$	0.7	21	25.8	5
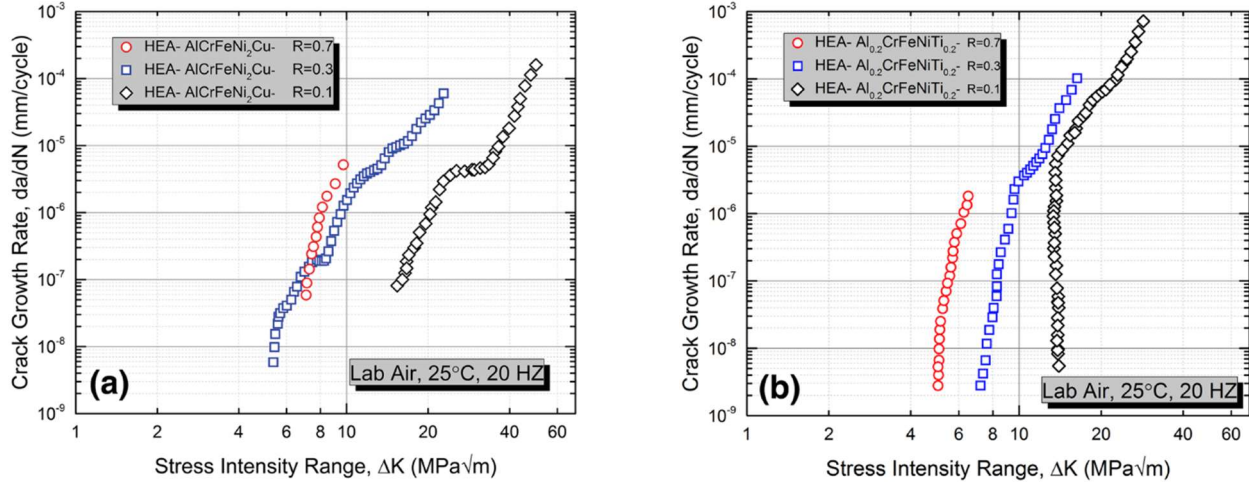
Figure 2.3: Fatigue crack growth rate over the stress intensity range for $AlCrFeNi_2Cu$ and $Al_{0.2}CrFeNiTi_{0.2}$ by Seifi *et al*. Tests were performed with 20 Hz at room temperature with R-ratios of 0.1, 0.3, and 0.7. **(a)** The fatigue threshold for $AlCrFeNi_2Cu$ tested under these conditions was found to be $\Delta K_{TH} \sim 17\ MPa\sqrt{m}$, $\Delta K_{TH} \sim 5\ MPa\sqrt{m}$, and $\Delta K_{TH} \sim 7\ MPa\sqrt{m}$, respectively. Those of $Al_{0.2}CrFeNiTi_{0.2}$ were similar, as shown in **(b)**: $\Delta K_{TH} \sim 16\ MPa\sqrt{m}$, $\Delta K_{TH} \sim 7\ MPa\sqrt{m}$, and $\Delta K_{TH} \sim 5\ MPa\sqrt{m}$ at the corresponding R-ratios [34].

Both alloy systems were found to exhibit remarkably high fatigue thresholds of 16 MPa√m and 17 MPa√m for Al$_{0.2}$CrFeNiTi$_{0.2}$ and AlCrFeNi$_2$ Cu respectively at R-ratio = 0.1 with Paris slopes within the typical range of metals (3-6). These curves were both found to shift lower with increasing R-ratio, leading to a decrease in fatigue thresholds to 7 MPa√m and 5 MPa√m respectively and a significant increase in the Paris slopes up to 25.8 for the more-brittle Al$_{0.2}$CrFeNiTi$_{0.2}$ [34]. These characteristics coupled with observation of fracture surfaces that revealed a combination of ductile and brittle behavior lead the authors to draw parallels between the behavior of these two alloy systems and other metallic alloys, intermetallics, and metal matrix composite systems.

2.3. MECHANISTIC STUDIES

While the quantitative studies indicated fracture behaviors comparable to other commonly used metallic alloys proving the suitability of HEAs in structural capacities, further work was conducted to determine the mechanistic behavior responsible for the

observed fracture behavior. In addition to broadening our understanding of these alloys, characterization of the fracture mechanisms within the HEAs may allow for more refined and pointed generation of future alloy systems.

2.3.1. Nanotwinning

One most discussed mechanisms of interest in the field of structural HEAs is nanotwinning and the contribution it may make in the remarkable deformation behavior displayed by HEAs. Twinning is regularly observed in these materials in the form of post-processing recrystallization twins, a favorable phenomenon due to the low stacking fault energy of these multi-component systems. While deformation-induced nanotwinning has been observed in certain strain-activated conditions, the role nanotwinning may play is a topic of contention.

Transmission electron microscopy (TEM) imaging conducted by Tang *et al.* on post-fatigue samples revealed dense tangles of dislocations and nanotwins within the material [33]. Deformation nanotwinning would result in more twin boundaries, leading in turn to additional work hardening as they act as high-angle grain boundaries and the crack propagation was found to be crystallographic. The resulting decreased stress concentration increases the strength of the alloy and thus the fatigue endurance of the material. As such, nanotwinning was theorized to serve as the main deformation mechanism leading to the high endurance limits of this dual phase HEA as the low stacking fault energy due to Suzuki interactions as well as the high strength of HEAs favorably affect the formation of nanotwins [33]. Niendorf *et al.* further corroborate this theory of nanotwinning acting as an important deformation mechanism, particularly under in cryogenic conditions [36].

The nanotwinning observed by Tang *et al.* was found to consist of both deformation-induced nanotwins and processing-generated nanotwins; these observations align with the results of Hemphill *et al.* who found a large number of nanotwins present in the material after the cold rolling process [31-33]. Furthermore, Liu *et al.* attributed the large, uniform elongation observed in the tensile behavior to the ultrafine grain $Al_{0.3}CoCrFeNi$ to the dynamic Hall-Petch effect resulting from nanotwinning behavior in the FCC matrix phase of the alloy [34]. Liu *et al.* suggest this twinning propensity may further result in the excellent fatigue properties observed in the material by reducing the crack growth rate through nanotwin crack bridging in addition to the general work hardening-assisted fatigue life enhancement from nanotwin formation.

2.3.2. Planar Slip

While twinning may play a role in crack-deflection, other mechanisms have been investigated, particularly to explain the differences in fatigue behavior of the same material subject to different conditions. In addition to twins, Tang *et al.* observed strong evidence of slip lines and bands after a sufficient number of cycles in regions of high plastic deformation; these slip bands were described as potential sites of microcracking and crack propagation within these regions [33]. Interesting, Niendorf *et al.* further theorized that planarity slip may lead partially to the discovered partial deformation reversibility observed in the scrutinized TWIP-HEA which in turn may contribute to high fatigue limits [36].

2.3.3. Roughness-induced crack closure

Crack closure effects have further been suggested as the dominant mechanism responsible for the downward shift of the fatigue curve with increasing R-ratio. In metallic alloy systems, increasing load ratios often lead to reductions of fatigue thresholds coupled with an increase in the Paris exponent. Seifi *et al.* postulated that R-ratio dependency of HEAs reflected crack closure effects corresponding significant surface roughening at low R-ratios [35]. The smoother, less-deformed fracture surfaces would allow for greater physical contact of the crack flanks, leading to a reduction in the crack-tip opening displacement, thus preventing plastic grain deformation in the crack wake at cryogenic conditions resulting in increased fatigue-thresholds [37]. However, the degree to which this change may be attributable to crack-closure is unclear and warrants further investigation.

2.4. DISCUSSION

2.4.1. Importance of processing method

As shown by the work of Hemphill *et al.* and Tang *et al.*, particular microstructural characteristics of the alloy play a critical role on the overall performance of an HEA under fatigue conditions. Scanning electron microscopy (SEM) imaging of the fracture surfaces confirmed voids and/or inclusions were present in the fatigue-crack initiation region and likely propagated between pores [33]. As the theory of the weakest link suggests, stress concentrators and flaws (e.g. micro cracks, voids, impurities…) in the highly loaded gauge area of a specimen can drastically reduce its fatigue lifetime, holding true for HEAs both experimentally and computationally. In general, increased surface roughness due to local plastic deformation in turn generates points of stress concentration that further

facilitate crack initiation. Local plastic deformation may be introduced through a variety of mechanisms including but not limited to the effect of uneven thermal gradients during processing (such as casting) and cold-working; however, annealing and heat-treatment can alleviate its impact on the final specimen. This theory further explains the manner in which scatter of fatigue tests can be significantly decreased by using high-purity elements. In order to reach the theoretic upper bound endurance limits and further to decrease the scatter of test results, continual improvement of the manufacturing process is desirable [29,30]. In addition to preventing flaws, the tuning of other microstructural characteristics, such as grain size, can also be conducted through modification of the processing procedures to further improve the mechanical properties of these materials as shown by ultrafine grained HEA studies of Liu *et al* [34].

2.4.2. Comparisons to other metallic alloy systems

The fatigue properties of the investigated HEA systems were found to largely outperform most of the modern material compositions. This trend is particularly evident in the total-life tests when using the metric of the ratio between fatigue threshold and ultimate tensile stress for comparative purposes as shown in **Figure 2.4**. This comparison method was suggested by Seifi *et al.* to provide a more rounded evaluation of this mechanical property as materials demonstrating higher ultimate tensile stress often exhibit lower ductility was well [15,33,35]. High entropy alloys seem to outclass common metallic systems such as aluminum- and magnesium-based alloys and even some steels in this respect. In comparing endurance limits of the various metals, Tang *et al.* found that of the aluminum-variant HEA was elevated relative to steels and Ni-based superalloys and was only rivaled by the bulk metallic glasses (BMGs) which demonstrate undesirable brittleness compared to the ductility of HEAs; these results can be found in **Figure 2.5** [33]. Depending on the processing method, the endurance limit of $Al_{0.5}CoCrCuFeNi$ ranged between a stress amplitude of 275 and 550 MPa, while the steels and superalloys fell between 100 and 250 MPa depending on the alloy system.
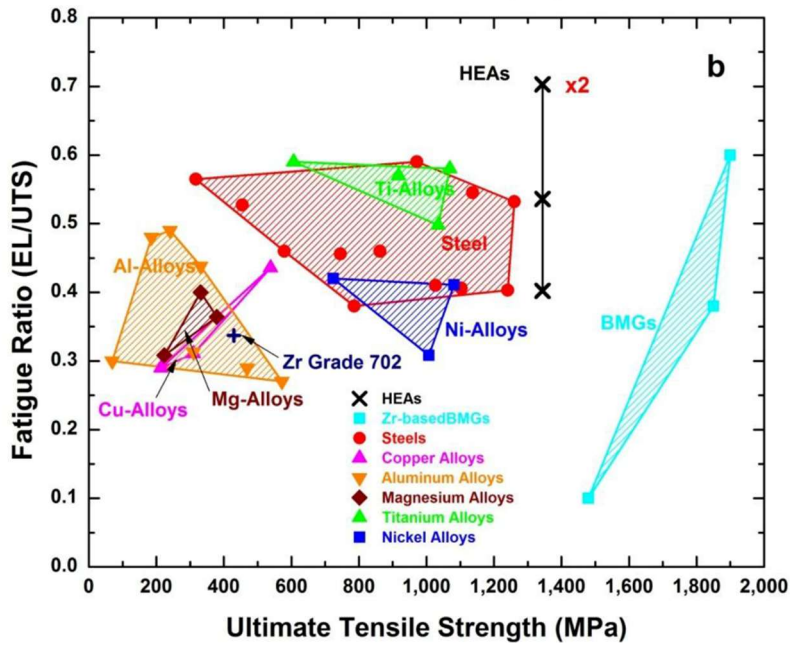
Figure 2.4: Plot depicting the relationship between the fatigue ratios and the ultimate tensile stresses of $Al_{0.5}CoCrCuFeNi$ and other common engineering alloys. The HEA was found to exhibit a range of fatigue behavior which was comparable to standard steels on the lower end of the spectrum while on the higher end, low-defect HEAs outclassed even bulk metallic glasses [33].
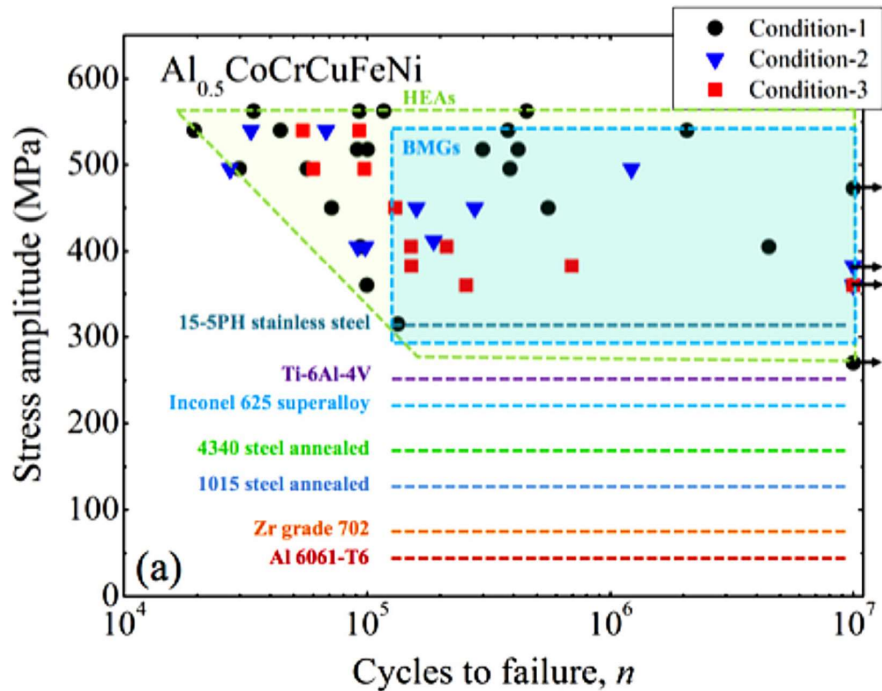
Figure 2.5: Comparison of the fatigue endurance limits at 10^7 cycles between the $Al_{0.5}CoCrCuFeNi$ and other conventional alloys. The HEA was found to outperform most of the common engineering materials though also displayed wide scatter depending on the precise processing conditions [33].

14

In the presence of a pre-existing flaw, the crack propagation behavior of the tested HEAs was found to demonstrate behavior either very comparable or superior to other commonly used structural and low-temperature steels depending on microstructure at an R-ratio of 0.1. The as-cast Al-variant compositions $Al_{0.2}CrFeNiTi_{0.2}$ and $AlCrFeNi_2Cu$ showed comparable Paris slopes of ~5 and 3.5 but elevated fatigue thresholds of 16 and 17 MPa respectively, which may be due to the as-cast microstructure of these systems [35]. While limited, the presented research suggests promising properties for possible future applications of HEAs in which fatigue may occur as HEAs seem to be a safer alternative for cutting-edge applications such as aerospace with excellent malleability and ductility coupled with high endurance limits [9,36], but much more work must be done to fill the large gaps of knowledge and understanding currently present in the literature.

2.4.3. Potential directions for study

In general, the dominant conclusion reached upon surveying the current body of literature is the lack of information available with ample room for further investigation in nearly all respects from compositional and microstructural alterations to testing conditions. Only a very small fraction of the growing HEA family has been tested, and of those, the specimens have varied in processing, microstructure and test method, making proper comparison between the various HEAs very difficult.

With regards to methodology, several conclusions regarding testing procedure going forward have arisen from the aforementioned works. The work of Hemphill *et al.* and Tang *et al.* stress the importance of sample preparation with high purity elements and defect-removal for optimal and consistent performance with minimal scatter [31-33]. The authors further discussed the importance of implementing tensile-fatigue testing – in contrast to the performed four-point bend tests – to allow for ease of comparison of fatigue test data with that of common engineering alloys and propose future work focusing on this method. Niendorf *et al.* plan to further this research into the effects of initially induced defects within the context of TRIP-HEAs and their performance under high-cycle fatigue conditions [36].

Beyond alteration to specimen testing procedure, several specific avenues of research have been proposed to help bridge some of the gaps between the works presented here and to further explore the mechanisms underlaying the fatigue behavior of these alloys. For example, Seifi *et al.* plan to further examine the temperature dependence of the two phases $Al_{0.2}$ $CrFeNiTi_{0.2}$ and $AlCrFeNi_2Cu$ alloy systems [34,35]. However, they plan give special attention to the bcc brittle-to-ductile transition at higher temperatures and the

resulting impact on the fatigue-crack growth rate and thus   the potential for high-temperature fatigue-related applications for HEAs rather than low temperature testing.

There also exists room for improvement outside of the laboratory within the theoretical and computational realm, but the development of these sub-fields require more empirical work to be conducted and to serve as the foundation for future predictions. Preliminary computational models seem to be able to forecast tendencies of the fatigue-behavior, but require additional low-scatter data for accurate results and are currently only applicable to a severely small range of the HEA family; Hemphill *et al.* applied a Weibull mixture model predicted an endurance limit of 858 MPa for the $Al_{0.5}$ CoCrCuFeNi alloy, while the test results found it to be between 540 and 945 MPa [31,32]. Tang *et al.* have further built on this work, having shown acceptable predictions of the fatigue lifetime with a random endurance limit model, but to develop more precise models, additional low-scatter test results are needed [33]. Additionally, the mechanisms underlying the fatigue behavior of HEAs remain somewhat murky, hampering understanding of the fundamental nature of this mechanical behavior. Future research is needed to fully understand the microstructural role and impact on the fatigue behavior of HEAs to utilize their outstanding mechanical behavior in modern applications.

Chapter 3
Fatigue Characterization of the Cantor Alloy

Our society's demand for structural materials tailored to fit an increasingly wide range of applications, coupled with the development of a vast array of processing techniques, have spurred great interest in alloys that flout convention and may exhibit hitherto unknown yet desirable properties. To help fill this role, high-entropy alloys and the related 'medium-entropy alloys' (MEAs; comprising 3 or 4 elements in near-equiatomic concentrations) are being examined in earnest as a class of seemingly unlimited new structural materials based on the belief that many new alloys with useful properties may be discovered [1-5,7-12,36-43]. One of the most prominent sub-classes of HEA and MEA alloy families is that of the CrCoNi system. Indeed, the five-component equiatomic CrMnFeCoNi alloy, first described by Cantor in 2004 [1], is a single-phase face-centered cubic solid solution with remarkable mechanical properties. Specifically, the alloy displays tensile strength levels of ~1 GPa associated with significant strain hardening, excellent ductility (~60-70%) and exceptional fracture toughness (KJIc > 200 MPa√m) [4,6,8,36-38]; moreover, these properties tend to improve with decrease in temperature between ambient and 77 K, i.e., they display damage-tolerant properties that tend to run counter to the vast majority of metal alloys that show a propensity for increasingly brittle behavior at cryogenic temperatures [4,8,11,44].

Whereas good strength and toughness are invariably vital characteristics for a structural material, resistance to fatigue is often the limiting mechanical property, as this generally determines the engineering lifetime of a given component for many applications. As noted above, the mechanical properties of the CrMnFeCoNi alloy have been well characterized under monotonic loading [4,7,8,10,11,36,38], but there is little information to date how this alloy performs under cyclic loads. As a potential new class of structural materials, it is clearly important that the fatigue behavior of HEAs and the various factors that may affect it, such as grain size and temperature dependence, are clearly understood. To date there have been only a few studies on the fatigue of HEAs, but these have generally been focused on as-cast, rather than recrystallized materials with uniform grain size; moreover, they have all been performed at room temperature [31,35,45]. Thus I sought to characterize the high-cycle fatigue-crack propagation behavior of the CrMnFeCoNi alloy, using material with a uniform recrystallized grain size. Furthermore, as this alloy is particularly notable for its cryogenic damage-tolerant properties, I performed these experiments at both room temperature and 198K, to evaluate how the improved strength, ductility and toughness of the material at cryogenic temperatures translates into its fatigue-crack growth resistance.

3.1. METHODS AND MATERIALS

An ingot of the CrMnFeCoNi alloy was produced at the Ruhr-University, Bochum, through vacuum induction melting and casting into a cylindrical mold. The ingot was then sealed in a quartz tube and thermally homogenized at 1473 K for 48 hr. Subsequently, the homogenized rod was rotary swaged at room temperature to reduce its diameter from 40 to ~16.5 mm before being recrystallized at 1073 K for 1 h, yielding a grain size of 7 ± 3 μm with a random orientation distribution [46]. The rod was then sliced into disc-shaped compact-tension (DC(T)) samples, in accordance with ASTM standard E1820 [47], using electrical discharge machining. 27 samples ($N = 27$) were machined with a width, W of 12.5 mm and thickness, B of 6 mm; notches were cut with depths varying from $a_0 = 3.6$ to 5.1 mm, corresponding to initial a_0/W ratios of ~0.28 to 0.4, respectively, and with notch root radii of ~100 μm.

The faces of all samples were metallographically polished using silicon carbide paper to a final 1 μm surface finish to allow accurate crack-length measurements on the surface of the samples using optical microscopy techniques. To allow continuous monitoring of the crack growth rate during testing, a linear patterned strain gauge (Vishay Precision Group, Raleigh, NC, USA) was applied to the back-face of each specimen: model EA-06-031DE-350 gauges were used for tests at 293 K or 198 K and model WK-13-031DE-350 gauges at 77 K, the latter to permit accurate readings in the deep-cryogen environment. The strain gauges were wired into a Wheatstone bridge to amply the signal for accurate monitoring. Crack lengths were calculated from the strain gauge readings during the elastic unloading portion of each cycle using the compliance expression for the DC(T) sample with back-face strain, as described by Ritchie *et al.* [48]:

$$a/W = 0.796239 + 5.40205u - 103.821u^2 + 714.676u^3 - 2603.44u^4 + 4829.01u^5 - 3578.51u^6 \quad , \qquad (1)$$

where
$$u = \frac{1}{\sqrt{-EBCW}+1} \quad . \qquad (2)$$

Here E corresponds to the Young's modulus of the material, and C represents the compliance calculated as the reciprocal from the unloading slope of the samples during testing. This calibration is considered valid for the range $0.3 \leq a/W \leq 0.8$; all samples were within this range for the entire duration of testing to ensure measurement validity.

Before testing, all samples were fatigue pre-cracked in ambient conditions using an electro-servo hydraulic MTS testing machine (MTS Corporation, Eden Prairie, MN, USA) controlled by an Instron 8800 digital controller (Instron Corporation, Norwood, MA, USA). Fatigue pre-cracking was conducted under load control (tension-tension loading)

within a stress-intensity range, $\Delta K = K_{max} - K_{min}$, between 8 to 10 MPa√m at a constant sinusoidal frequency, f, of 25 Hz and a load ratio, $R = 0.1$, where R is the ratio of minimum to maximum load. For tests conducted at higher R, further pre-cracking was conducted, increasing the load ratio of pre-cracking in a stepwise manner until the testing R was matched in order to avoid excessive plasticity effects at the start of testing. The back-face strain gauges were calibrated and balanced at zero-load to ensure residual strain from mounting would not affect crack-length measurement, which was further verified during pre-cracking by optically checking both sides of the samples for crack length and linearity. Final overall pre-crack lengths including notches ranged from $a = 3.7$ mm to 5.17 mm ($a/W \sim 0.3$-0.41), all in accordance with ASTM 647 [49,50]. Images of components of the experimental set-up may be viewed in **Figure 3.1**.

Figure 3.1: Images of sample preparation and mounting in the Instron load frame. Clockwise from left: Wheatstone bridge consisting of three 350 Ω for signal amplification, sample with attached strain gauge and full wiring, side view of prepared samples, and sample mounted in load frame.

Fatigue-crack growth tests were performed under sinusoidal cyclic loading at $f = 25$ Hz at one of three constant load ratios of $R = 0.1$, 0.4, and 0.7 in three different temperature environments: room temperature air (293 K), dry ice/ethanol bath (198 K), and liquid nitrogen (LN₂) (77 K); thus yielding a total of 9 testing condition sets. All fatigue-crack propagation testing was performed under load-shedding or constant load control conditions. Near-threshold crack-growth rates were determined under load-shedding conditions, which was automated to decrease the load at a rate such that the normalized

K-gradient remains above -0.08 mm^{-1}, as recommended in ASTM E647 [51]. ΔK_{TH} fatigue threshold stress-intensity values were determined as the maximum value of the stress-intensity range, ΔK, to give a growth rate approaching 10^{-11} m/cycle. Higher regions of the crack-growth curves were characterized under constant load conditions, in which the amplitude of the sine wave is held constant, effectively increasing the stress-intensity range as the crack grows, while the rest of the fatigue curve was determined by an overlap of the two methods. To obtain the moderate cryogenic test conditions, a dry ice/ethanol bath was prepared and maintained at 198 K for the duration of the test. To obtain the low cryogenic test conditions, a LN$_2$ bath was continually maintained to keep the sample submerged throughout testing. Samples subjected to 198 K and 77 K conditions were tested in a continuous manner at this temperature to avoid potential thermal cycling effects [52]. For all samples, crack length verification by optical microscopy was carried out after testing after samples had been brought back up to room temperatures in an ambient temperature ethanol bath to avoid oxidation of the fracture surfaces.

To determine the microstructural mechanisms controlling the propagation of the fatigue cracks in this alloy and to investigate the nature of the crack paths (**Chapter 4**), select samples were sliced longitudinally through the center for back-scattered electron (BSE) and electron backscatter diffraction (EBSD) analyses, performed using a Zeiss LEO 1525 field-emission scanning electron microscope (FE-SEM, Carl Zeiss, Oberkochen, Germany) operated at 20 kV using a TEAMTM EDAX analysis system (Ametek EDAX, Mahwah, NJ, USA). To perform fractography analyses, samples from both temperatures were subsequently quasi-statically loaded to complete failure to have unrestricted access to their fracture surfaces. In addition to the microscopic analysis with the Zeiss-SEM, fracture surface characterization was also performed using a JSM-7500F SEM (JEOL USA, Arvada, CO, USA) operated at 5-15 kV in secondary electron (SE) mode. Further BSE and EBSD imaging was conducted with an FEI Strata DB235 SEM (FEI Company, Hillsboro, OR, USA) operated at 20 kV using a TEAMTM EDAX analysis system (Ametek EDAX, Mahwah, NJ, USA) with step sizes of 0.12-0.1 μm. Post-processing of these EBSD images was conducted using OIM Analysis v6 software (Ametek EDAX, Mahwah, NJ, USA).

3.2. RESULTS

3.2.1. Fatigue testing at 293 K and 198 K with R = 0.1

Prior studies conducted on the equiatomic, single-phase fcc CrMnFeCoNi alloy with the same microstructure have found it to display mechanical properties that either remain consistent or improve as the testing temperature is lowered into the cryogenic regime. In this regard, both strength and ductility of the material are particularly notable for their

strong temperature dependence; the transition from 293 K to 198 K yields an increase in ultimate tensile strength from ~760 MPa to ~925 MPa with a similar increase in yield strength from ~410 MPa to ~520 MPa while its ductility increases from ~0.6 to ~0.7 [8]. Over the same temperature range, the Young's modulus [53,54], toughness and strain hardening exponent remain relatively unchanged. While both Young's modulus, E, and fracture toughness, K_{JIc}, increase slightly from 202 GPa to 209 GPa and from 217 MPa√m to 221 MPa√m, respectively, the strain hardening exponent of the material remains consistently high at ~0.4 [8] These trends, displayed by strength, modulus, toughness and strain hardening coefficient measurements, have been found to continue as the temperature is further decreased to 77 K.
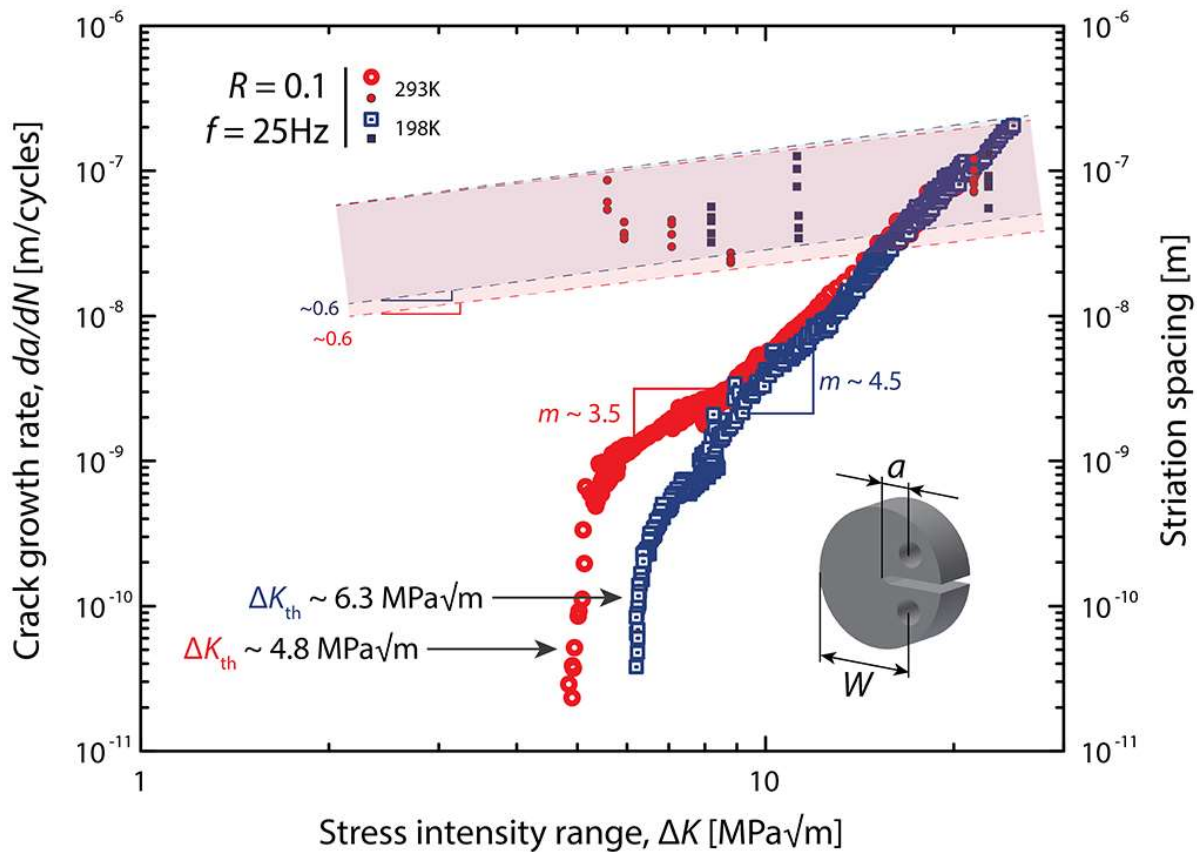
Figure 3.2: Fatigue-crack growth behavior of the CrMnFeCoNi alloy, tested at a load ratio R of 0.1 at 293 K and 198 K. A direct comparison of the fatigue-crack growth curves, as a function of the stress-intensity range, ΔK, at both temperatures tested on disc-shaped compact-tension (DC(T)) samples at a frequency of $f = 25$ Hz reveal a clear shift in the fatigue threshold, increasing some 30%, from ~4.8 MPa√m to ~6.3 MPa√m, as the temperature was reduced from ambient to cryogenic conditions. The Paris exponent m was found to change from 3.5 at 293 K to 4.5 at 198K. The smaller sized, solid symbols indicate the corresponding variation, as a function of ΔK, in local crack-growth rates, which were estimated from striation spacing measurements on the scanning electron microscopy images of the fracture surfaces.

Here, the fatigue-crack growth rates, da/dN, of the alloy, for tests at 293 K in air and at 198 K in dry ice/ethanol, are plotted in **Fig. 3.2** as a function of the applied stress-intensity range, ΔK. Although crack-propagation rates are comparable in the mid-range of growth rates above ~10^{-8} m/cycle with only a modest change of the Paris exponent m from 3.5 at 293K to 4.5 at 198 K, near-threshold growth rates and the value of the fatigue threshold, ΔK_{TH}, of this alloy are markedly improved at cryogenic temperatures. Specifically, growth rates are lowered by up to an order of magnitude, and threshold ΔK_{TH} values are increased by ~30%, from ~4.8 MPa√m to ~6.3 MPa√m, with decrease in temperature from 293 K to 198 K.

At higher growth rates, traditional fatigue striations are visible on the fatigue fracture surfaces of this high-entropy alloy (**Fig. 3.3**). These features are rather rounded and characteristic of ductile striations. To analyze these features, I screened the fracture surfaces of four samples specifically for fatigue striations, two each from the 198 K and 293 K crack-growth experiments. Sampling was conducted at intervals of 1 mm, beginning 1 mm from the notch along the width of the sample until the overload region along the centerline of the sample, with multiple images taken at each location to check for consistency. While the fatigue striations at growth rates near the threshold are hard to detect and cannot often be easily distinguished from slip steps, e.g., careful investigation of the fatigue striations, as shown on the example of a sample tested at ΔK ~ 21.5 MPa√m (**Fig. 3.3**) shows good agreement (**Fig. 3.2**) between their spacing and the macroscopic growth rate of ~10^{-7} m/cycle for both temperatures, as shown in **Fig. 3.2**. **Fig. 3.2** also clearly indicates the actual correspondence of striation spacing as a function of ΔK of the local crack-growth rates and the macroscopic growth rates measured at both temperatures. At lower values of ΔK, the width of fatigue striations begins to diverge from the macroscopic growth rates, behavior which is indicative of the non-uniform crack propagation along the crack front at low growth rates as the crack advances in an incremental fashion. Overall, striation spacing measurements for both sets of samples displayed the generally linear trend characteristic of the approximate first-order description of macroscopic crack-growth rate behavior, albeit with scatter due to variability in measurements.
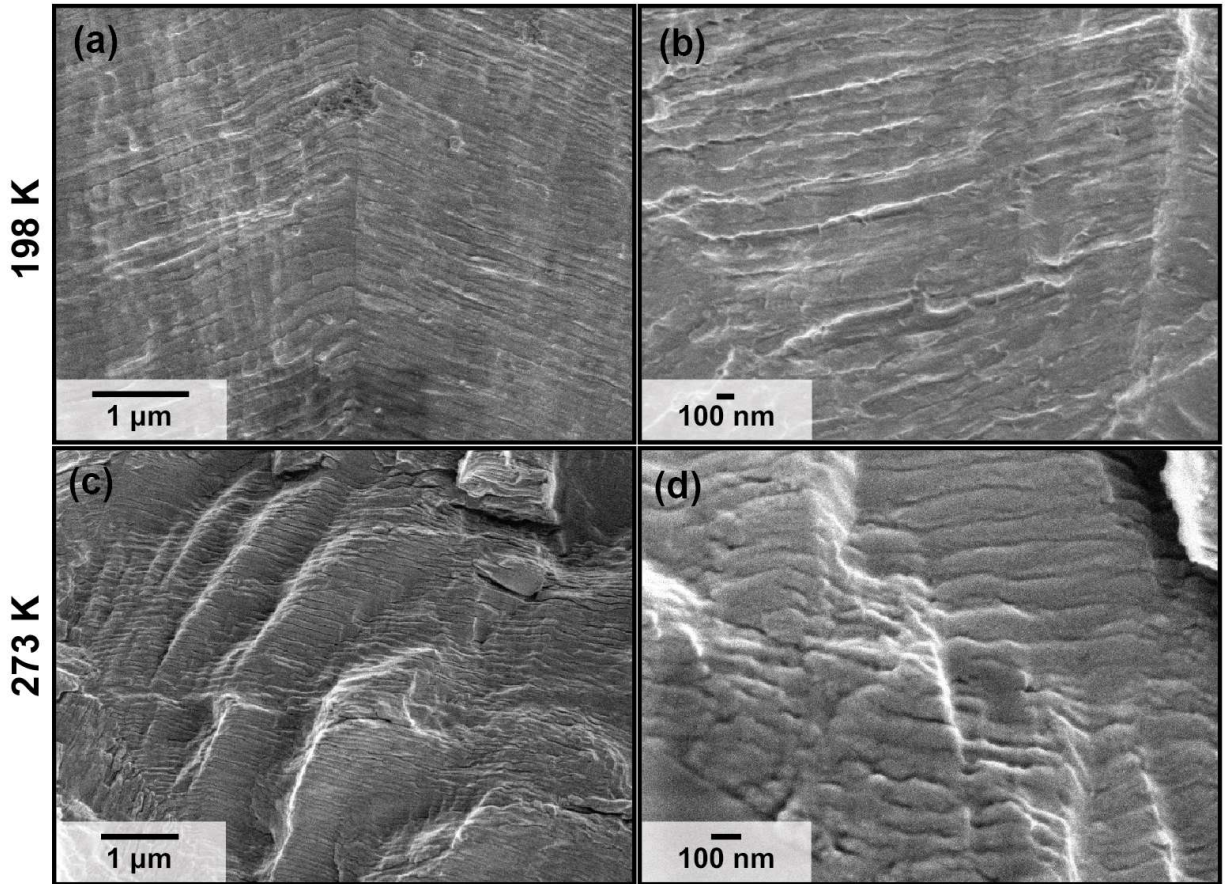
Figure 3.3: High magnification SEM of fracture surfaces at comparable $\Delta K \sim 20$ MPa√m. (a),(b) depict 198 K tested sample in the region $\Delta K \sim 22.7$ MPa√m while (c),(d) depict the ambient 293 K tested sample in the region $\Delta K \sim 21.6$ MPa√m to allow comparison between the two sets of images under similar loading conditions. At this ΔK, the measured crack growth rate was $\sim 1\times10^{-7}$ m/cycle for both temperature regimes, so we would expect fatigue striations to have a width of ~100 nm. This value corresponded well with the observed striation rate in both sets of samples, with average widths of $\sim 8\times10^{-8}$ m and $\sim 9\times10^{-8}$ for 198 K and 293 K respectively While the striation size was similar, the shape differed drastically between the two temperatures. While samples tested at 198 K displayed sharp, angular striations on flatter surfaces, the samples tested at 293 K show far more irregular, rounded striations.

3.2.1. Fatigue testing at R = 0.4 and 0.7

Upon the conclusion of testing at $R = 0.1$, trials at $R = 0.4$ and 0.7 commenced. Additionally, the temperature range of testing was extended down to 77 K with sampled immersion in cryogenic LN_2. However, due to testing limitations, LN_2 trials were limited to testing under constant load conditions, and thus the linear portion of the Paris regime; no threshold data was collected at this temperature. The summarized data may be viewed in **Figure 3.4** and **Table 3.1**

23
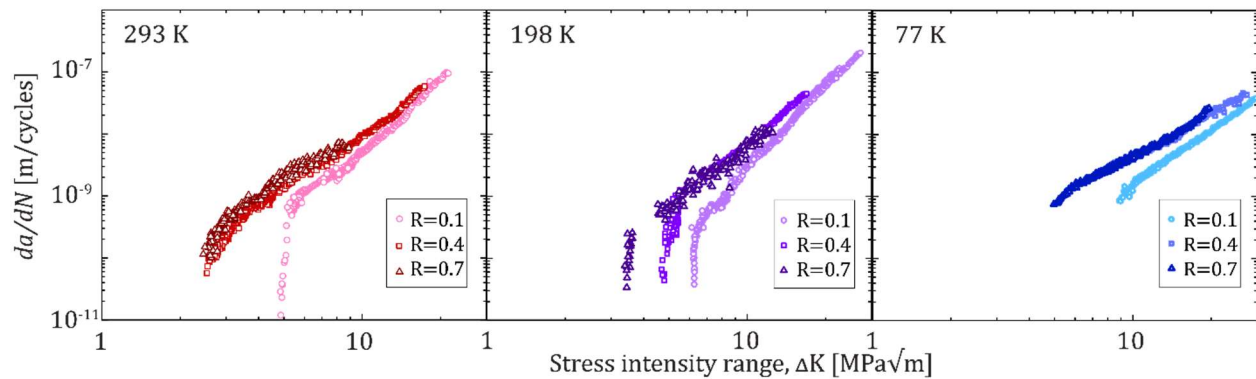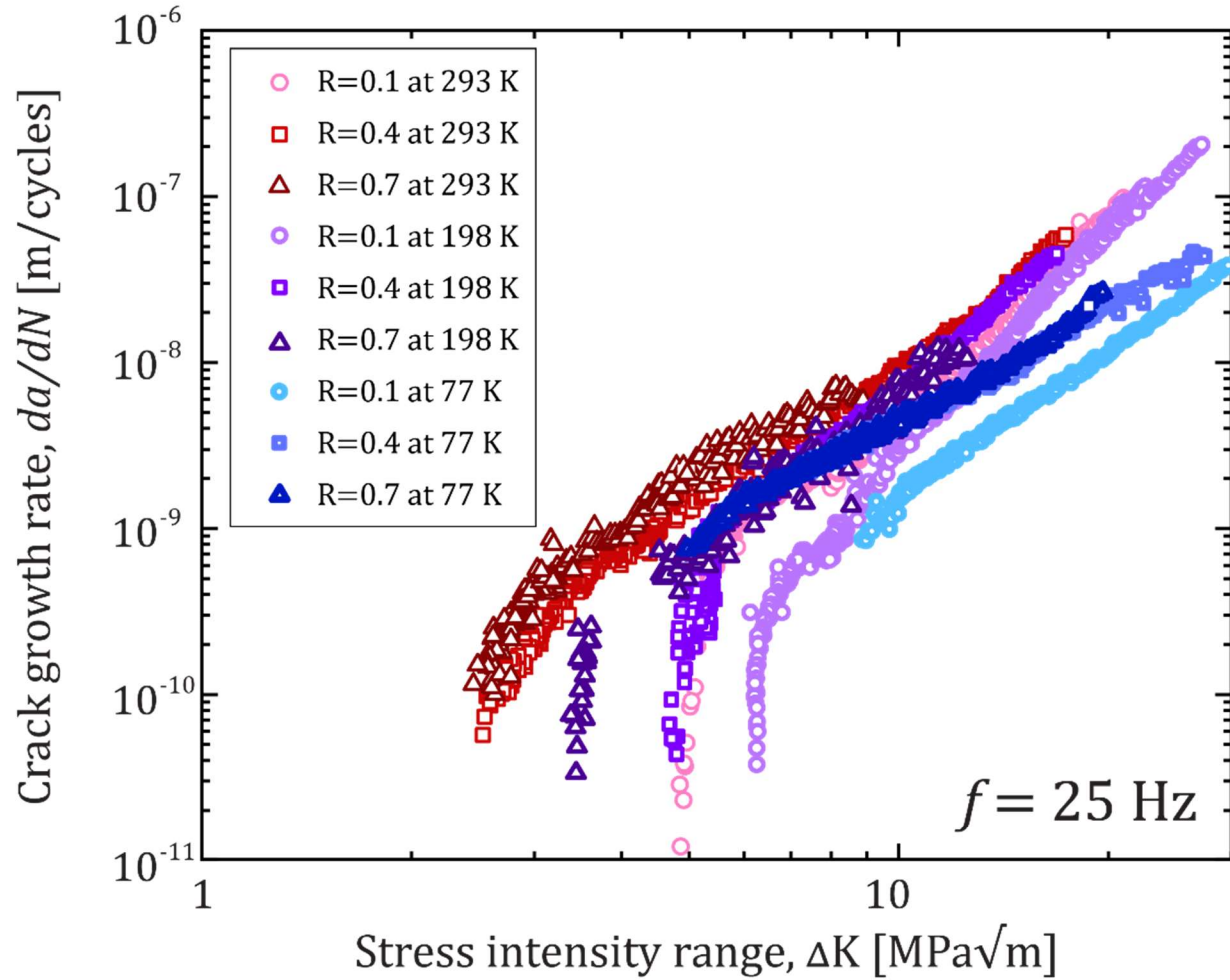
Figure 3.4: Fatigue crack growth rates as a function of the stress-intensity range for the Cantor alloy under various testing conditions. Testing was conducted over three temperature ranges between ambient (298 K) and liquid-nitrogen temperature (77 K) at *R* = 0.1, 0.4, and 0.7 at 25 Hz. Tests at 77 K were limited to the upper region of the mid-growth rate regime while testing at 293 K and 198 K continued until the fatigue threshold stress intensity was reached. A direct comparison of the crack-propagation curves characterizing these various testing parameters indicates a clear upwards shift in the value of the ⊘K_{TH} threshold as both temperature and load ratio were decreased.

Table 3.1: Summary of fatigue-crack growth and threshold data, as shown in **Fig. 3.4**

Temperature	Load Ratio (R)	Paris Law exponent (m)	Threshold (ΔK_{TH}) [MPa$\sqrt{\text{m}}$]
293 K	0.1	3.5	4.8
	0.4	2.8	2.6
	0.7	2.6	2.5
198 K	0.1	4.5	6.3
	0.4	3.4	4.8
	0.7	3.1	3.5
77 K	0.1	2.9	
	0.4	2.3	
	0.7	2.3	

As indicated by the data, for the mid-range of growth rates above 10^{-9} m/cycle, the Paris law exponents for all temperatures and load ratios were largely in the characteristic range of $m \sim 2$ to 4, although in general there was a trend of increasing fatigue-crack growth resistance, i.e., lower growth rates, at a given ΔK, and higher values of the fatigue ΔK_{TH} thresholds, at the lower temperatures. Indeed, ΔK_{TH} values, which ranged from 6.3 to 2.5 MPa$\sqrt{\text{m}}$ at load ratios between 0.1 and 0.7 were, respectively, 31% and 12% higher at 198 K as compared to 293. Additionally, there was a marked effect of load ratio on crack-growth rates and ΔK_{TH} threshold values with increasing load ratios which became more prominent at near-threshold levels. Specifically, ΔK_{TH} threshold values are 2-3 times lower at $R = 0.7$ compared to $R = 0.1$. Such load-ratio dependent behavior is typical of most metallic alloys [51] and can generally be related to crack-tip shielding from fatigue crack closure effects [55], as further discussed in **Chapter 4**.

Upon investigation of the fracture surfaces, traditional striation features could be observed at $R = 0.4$ and $R = 0.7$ samples, with particularly clear visibility at high crack growth rates. As with the striations observed in $R = 0.1$ tested samples, the striation width of these striations generally agreed with the predicted crack growth rate in these regions. Examples of observed striations of samples tested at 198 K are shown in **Figure 3.5.** While visible at all values of R, increasing R seemed to correlate with increasing prominence of striations which may be due to the greater plastic deformation of the sample with higher load ratio. As with the $R = 0.1$ samples, as ΔK decreased, the striation width began to deviate from the calculated crack growth rate and to become obscured by other surface features, further discussed in **Chapter 4**.
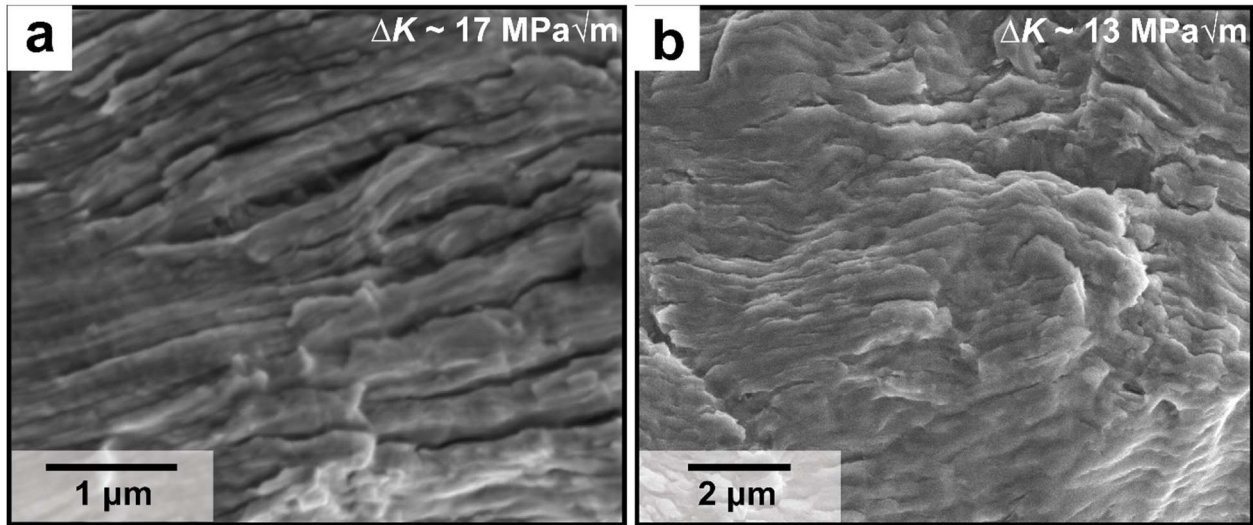
Figure 3.5: Example of fatigue striations observed in the high growth rate region of samples tested at 198 K. (a) and (b) depict samples fatigued at *R* = 0.4 and 0.7 respectively. Each image depicts striations of width on the order of the expected fatigue crack growth rate.

While these results satisfactorily summarize the basic fatigue data of the Cantor alloy at ambient and low temperature ranges, this information does not explain 'how' or 'why' the Cantor alloy may demonstrate this temperature dependent shift in fatigue behavior. As such, mechanistic studies were called for to explain these shifts and thus to potentially shed light on future alloy design.

Chapter 4
Mechanistic Studies of Fatigue in the Cantor Alloy

4.1. THRESHOLD ANAYSIS

The most prevalent reason for the marked effect of load ratio on fatigue-crack growth rates, especially at near-threshold levels, is that of crack closure. As this phenomenon is dominated by shielding effects due to wedging effects between the crack flanks, e.g., from corrosion debris (oxide-induced crack closure) and/or from crack surface asperities (roughness-induced crack closure), which act to reduce the effective stress-intensity range actually experienced at the crack tip, crack closure is exacerbated at low ΔK levels, where the cyclic crack-tip opening displacements (CTODs) are small and become comparable in dimension to the thickness of the "wedge", yet minimized at high positive load ratios where the minimum opening displacements are much larger, specifically where $K_{min} > K_{cl}$. On the simple assumption that the value of the closure stress intensity K_{cl}, and the effective stress intensity range at the threshold $\Delta K_{eff,TH}$ are nominally constant and independent of R, we would expect the measured variation in ΔK_{TH} thresholds to follow "Schmidt and Paris type" behavior [59]. Specifically, below a critical load ratio where $K_{cl} = K_{min}$ (usually on the order of R ~ 0.4-0.5), the ΔK_{TH} threshold should decrease with increasing R whereas the threshold K_{max} should remain roughly constant (this is the regime where closure is active as $K_{cl} > K_{min}$); above this critical R value though (where closure is inactive as $K_{cl} < K_{min}$), the value of ΔK_{TH} threshold should reach a lower-bound "plateau whereas the threshold K_{max} should increase as R tends to unity. A plot of ΔK_{TH} and K_{max} vs. R may be viewed in **Fig. 4.1**; although I have only tested three different load ratios at each temperature, these measurements are still useful to determining if the Cantor alloy's fatigue behavior roughly follows these crack closure related trends described by Schmidt and Paris.

Shown in **Fig 4.1**, the threshold data for this high-entropy alloy are not inconsistent with this hypothesis. As previously discussed, lowered temperature was found to have a pronounced impact on the stress intensity range at which a 'threshold' point of arrested crack growth was reached, particularly evident in samples tested at R = 0.4. Samples tested under ambient conditions at 293 K exhibited the aforementioned 'plateau' effect at load ratios of $R \geq 0.4$, staying roughly constant at $\Delta K_{TH} \approx 2.5$ MPa√m. However, this leveling-off behavior was not seen under cryogenic conditions among the R-ratios tested, with a continued decrease evident past R = 0.4. Following Schmidt and Paris, this would in turn indicate an upwards shift in the critical load ratio at which $K_{cl} = K_{min}$, though due to the small sampling of R-ratios, this point can only be said to be at $R > 0.4$.
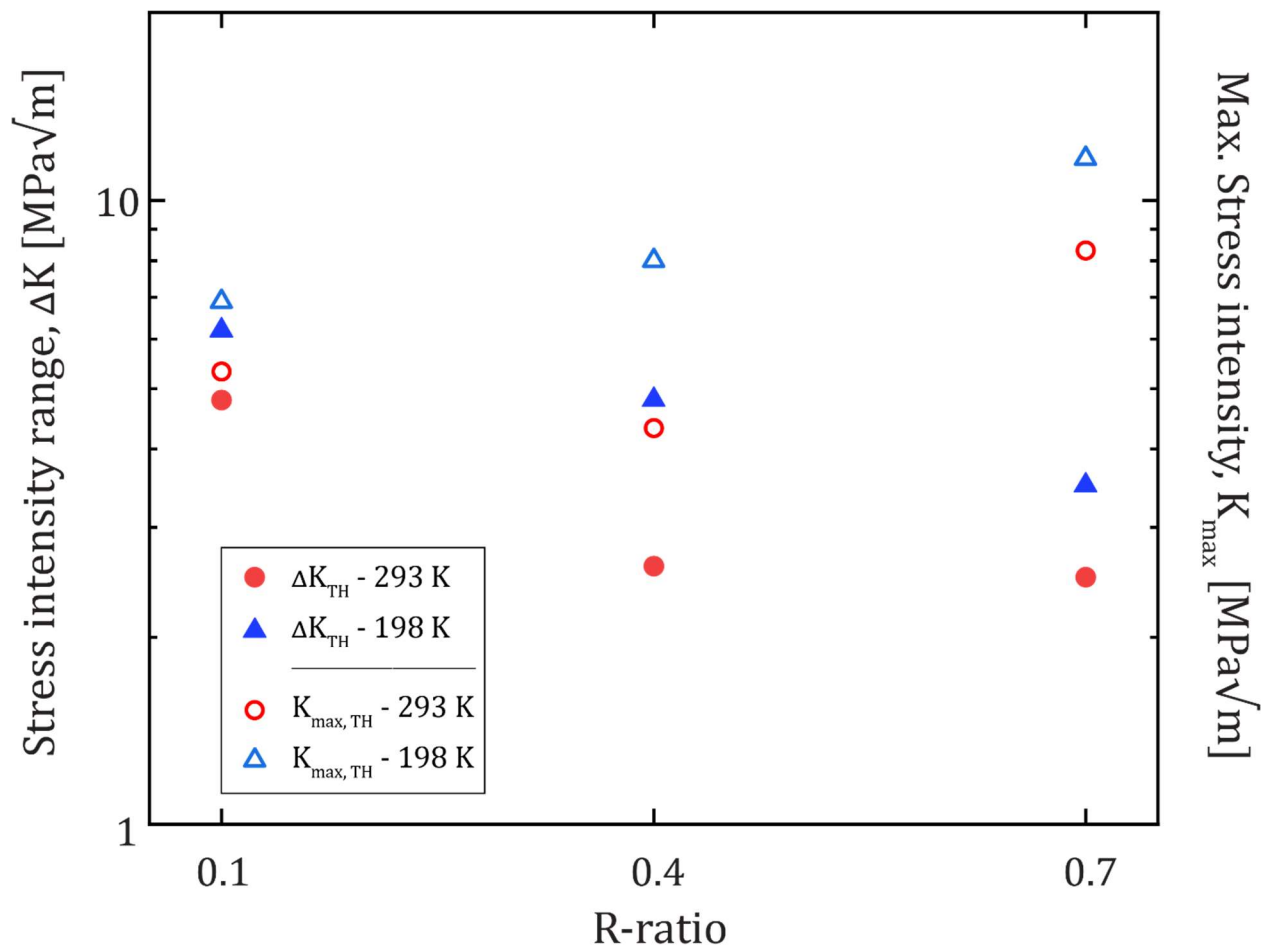
Figure 4.1: Plot of threshold ΔK_{TH} and $K_{TH,MAX}$ values of samples tested at 293 K and 198 K with respect to R-ratio

However, pertinent questions that remain are whether this closure affect can be associated with fracture surface roughness, which is the most prevalent form of fatigue crack closure in metallic materials, whether such phenomena can explain the observed increase in ΔK_{TH} thresholds in this HEA at cryogenic temperatures, and whether deformation twinning, which is so prevalent during overload fracture in this alloy at 77 K [8,10] plays an active role during fatigue-crack growth.

4.2. CRACK CLOSURE STUDIES

While the Schmidt and Paris approach provides a qualitative indicator that crack closure may be a contributing factor to the shift in threshold with temperature, a more quantitative approach was required. In order to calculate the degree to which crack-closure may be an active mechanism in near-threshold fatigue testing in the Cantor alloy, select near-threshold tested specimens were further subjected to limited loading and

unloading cycles to estimate the extent of crack closure from measurement of the stress intensity for crack closure, K_{cl}. This was used to estimate an effective stress-intensity range actually experienced at the crack tip, where $\Delta K_{eff} = K_{max} - K_{cl}$, where $K_{cl} > K_{min}$ (where $K_{cl} < K_{min}$, $\Delta K_{eff} = \Delta K$). Full details of these procedures can be found elsewhere [55,60]. These loading cycles were performed in incremental steps corresponding to an increase in ΔK of 0.5 MPa√m beginning at the threshold of the respective sample and the resultant position-displacement curves were plotted and analyzed for the distinctive 'kink' that indicates the popping open of the crack tip and thus K_{cl} for the analyzed region; this analysis, only the threshold region of the curve was examined. Additionally, approximations for the crack tip opening displacement (CTOD) at each threshold were calculated to compare with the approximate asperity sizes in the region. These results can be viewed in **Table 4.1**. Due to the lack of threshold data for 77 K, this analysis was limited to 293 K and 198 K tested samples.

Table 4.1: Summary of fatigue crack growth data with accompanying crack closure data

Temp.	Load Ratio (R)	Paris Law exponent (m)	Threshold (ΔK_{TH}) [MPa√m]	ΔCTOD [nm]	CTOD$_{max}$ [nm]	Crack Closure (K_{cl}) [MPa√m]	$\Delta K_{TH,eff}$ [MPa√m]
	0.1	3.5	4.8	130	160	1.38	3.95
293 K	0.4	2.8	2.6	40	105	-	2.6
	0.7	2.6	2.5	35	390	-	2.5
	0.1	4.5	6.3	170	210	2.15	4.85
198 K	0.4	3.4	4.8	100	275	2.7 - 3.4	4.6 - 5.3
	0.7	3.1	3.5	55	585	-	3.5
	0.1	2.9					
77 K	0.4	2.3					
	0.7	2.3					

As summarized in **Table 4.1**, crack closure levels are far higher at low load ratios as expected. Moreover, the effective $\Delta K_{eff,TH}$ thresholds appear to be roughly constant, again consistent with our observations of the marked effect of load ratio on the near-threshold fatigue behavior being associated with a crack closure effect. With regards to temperature trends, the data validates the prediction from the Schmidt and Paris analysis that the critical R-ratio for which $K_{cl} = K_{min}$ has shifted to a higher load ratio from $R \leq 4$ at 293 K to $4 \leq R \leq 7$ at 198 K, as crack closure is still observed at $R = 0.4$ but not at $R = 0.7$ in samples tested at 198 K. In both temperature ranges, crack closure appears to play a major role in the near-threshold fatigue behavior of this alloy.

4.3. CRACK PATH STUDIES

Examination of the crack paths was performed by sectioning samples at mid-thickness. At $R = 0.1$, samples tested at room temperature showed crack path behavior was primarily transgranular, particularly at high growth rates, with some minor intergranular crack growth at low and intermediate growth rates, as is apparent from the BSE images and EBSD scans in **Fig. 4.2**. The BSE images of the crack-tip region near the threshold at $\Delta K = 4.8$ MPa√m clearly indicate that the propagating crack runs through the grains and recrystallization twins and not along their boundaries. EBSD images taken from the wake of the crack at ΔK values of ~6.0 MPa√m and ~7.0 MPa√m show significant amounts of plastic deformation in the grains neighboring the crack flanks partly resulting from geometrically-necessary dislocations emitted from the crack tip during loading and unloading of the samples. Additionally, such plastically-deformed regions naturally occur as a result of local deviations from a straight crack path leading to physical contact of the mating crack surfaces resulting from small variations in the mode II displacements of the neighboring crack flanks. This is known as roughness-induced fatigue crack closure and acts to lower the crack-driving force experienced at the tip of the growing crack by effectively increasing the value of the minimum stress intensity in the fatigue cycle [56,57].

At room temperature, where the alloy has a lower strength compared to at 198 K, such closure can result in local plastically deformed regions near the propagated crack and particularly of the individual grains next to the crack flanks. This mechanism can to some extent account for the difference found in the fatigue threshold shown in **Fig. 3.2**. Interestingly, despite the relatively large stresses near the crack tip, deformation induced nano-scale twinning could not be observed by BSE and EBSD microscopy within these room temperature tested samples.
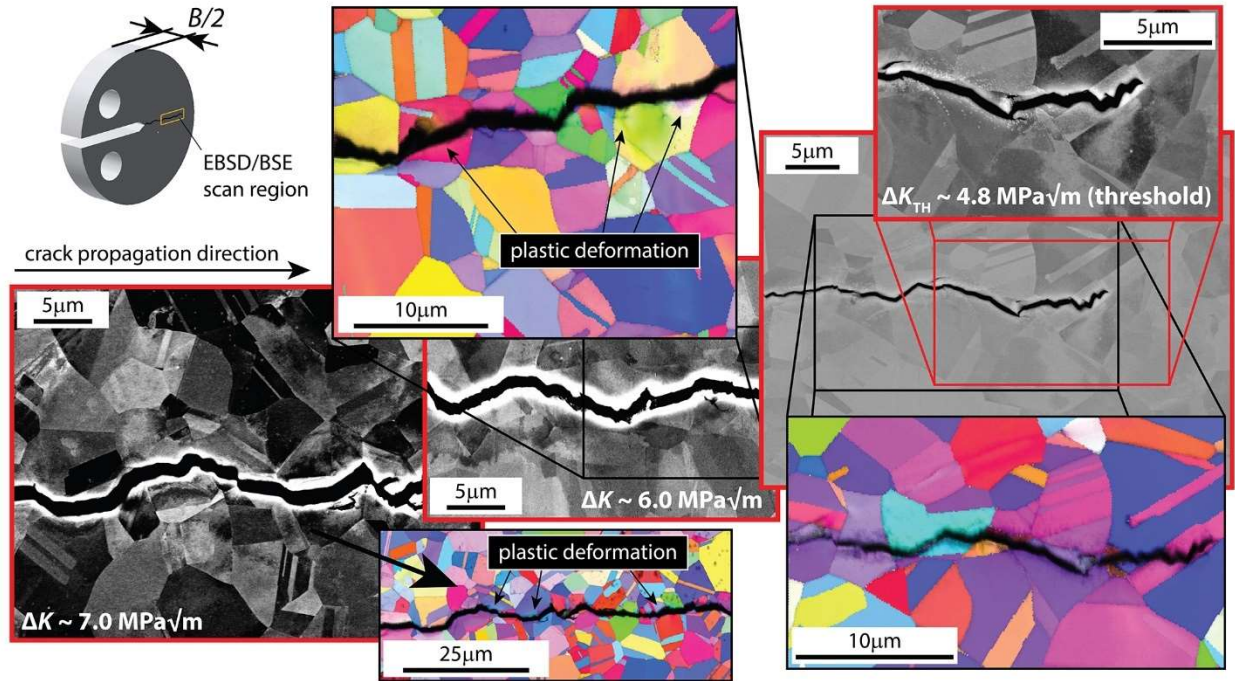
Figure 4.2: Crack path characterization of the CrMnFeCoNi alloy fatigue tested at 293 K and *R* = 0.1. Back-scattered electron (BSE) images and electron back-scatter diffraction (EBSD) scans taken at the mid-thickness of the samples near the threshold at ΔK = 4.8 MPa√m, specifically from the wake of the crack at ΔK values of ~6 and ~7 MPa√m, clearly show transgranular fracture as the dominant crack propagation mode. Images taken at the crack tip indicate that the crack propagated through the grains and recrystallization twins and not along their boundaries. EBSD scans taken from the wake of the propagating crack show plastically deformed region along the crack flanks resulting from physical contact between the mating crack surfaces and the lower strength of the alloy at room temperature.

Figure 4.3 displays the crack paths of the fatigue cracks at tested at *R* = 0.1 and in the 198 K temperature regime. Note that akin to the behavior at 293 K, we could not see evidence of nanoscale deformation twinning associated with the crack-growth mechanisms in our BSE and EBSD analyses, although as noted below, there appears to be evidence of the onset of twinning on the fracture surfaces. However, compared to the room-temperature behavior, both BSE images and EBSD scans clearly show significant amounts of intergranular fracture at this lower temperature; like at room temperature though, the presence of recrystallization twins did not appear to influence the crack trajectory. As a result of the intergranular crack propagation at the lower temperatures, the local crack path was naturally more deviated compared to that at room temperature, thereby giving rise to significantly more contact of the neighboring crack flanks to promote roughness-induced crack closure; this is consistent with the 30% higher threshold at 198 K, ΔK = 6.3 MPa√m, as compared to ΔK = 4.8 MPa√m at 293K; this crack closure mechanism operates particularly effectively within low stress-intensity range conditions like those of the near-threshold region [57,58]. Additionally, the higher strength at the lower temperature acts to limit the crack-tip opening displacements at a

given ΔK, as this displacement is proportional to $\Delta K^2/\sigma_y E$, where σ_y is the flow strength and E the Young's modulus; correspondingly, the generation of new crack surface during the opening of the crack in each cycle will be less effective.
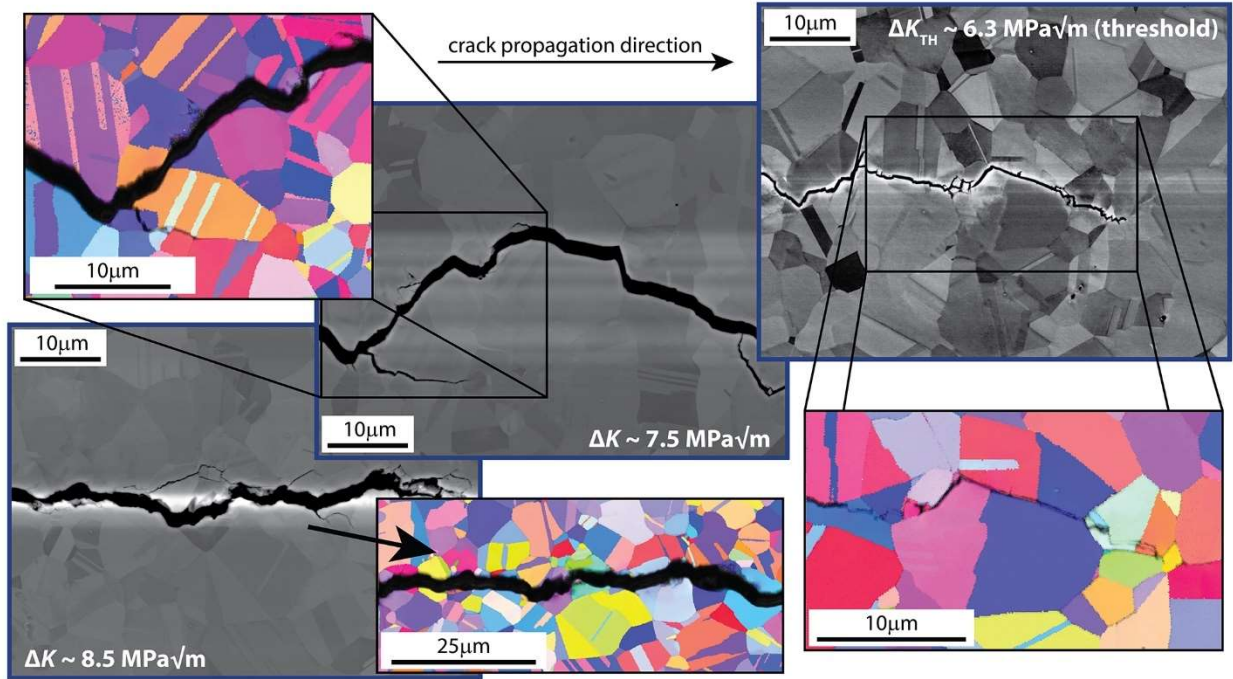
Figure 4.3: Crack path characterization of the CrMnFeCoNi alloy fatigue tested at 198 K and R = 0.1. In contrast to the behavior at room temperature (**Fig. 4.2**), both BSE images and EBSD scans revealed intergranular fracture as the dominant crack propagation mechanism at 198 K. The boundaries of the recrystallization twins do not appear to influence the path of the crack tip, as can be seen near the threshold at ΔK = 6.3 MPa√m and at higher growth rates at ΔK values of ~7.5 MPa√m and ~8.5 MPa√m; this is believed to be a result of the higher strength of the material at 198K, such that plastically deformed regions along the propagated crack do not to occur.

Together, these two sets of images lend strong evidence to a lack of twinning as a dominant mechanism in the fatigue behavior of these alloys; should deformation twinning be a factor in the temperature dependence of fatigue in this alloy, then their presence would have been noted along the crack path of samples tested at 198 K. Rather than deformation twins, potential regions of crack closure were noted, further indicating the likely dominance of this mechanism in the fatigue threshold shift. However, while deformation twinning does not likely play a role at the threshold, it does appear to become activated at sufficiently high ΔK (or, rather, K_{max}) and sufficiently low temperature. As displayed in **Fig. 4.4**, the samples tested in LN$_2$ at R= 0.1 and R = 0.7 subjected to high ΔK were both found to contain evidence of a small number of deformation twins that formed in grains along the crack path.
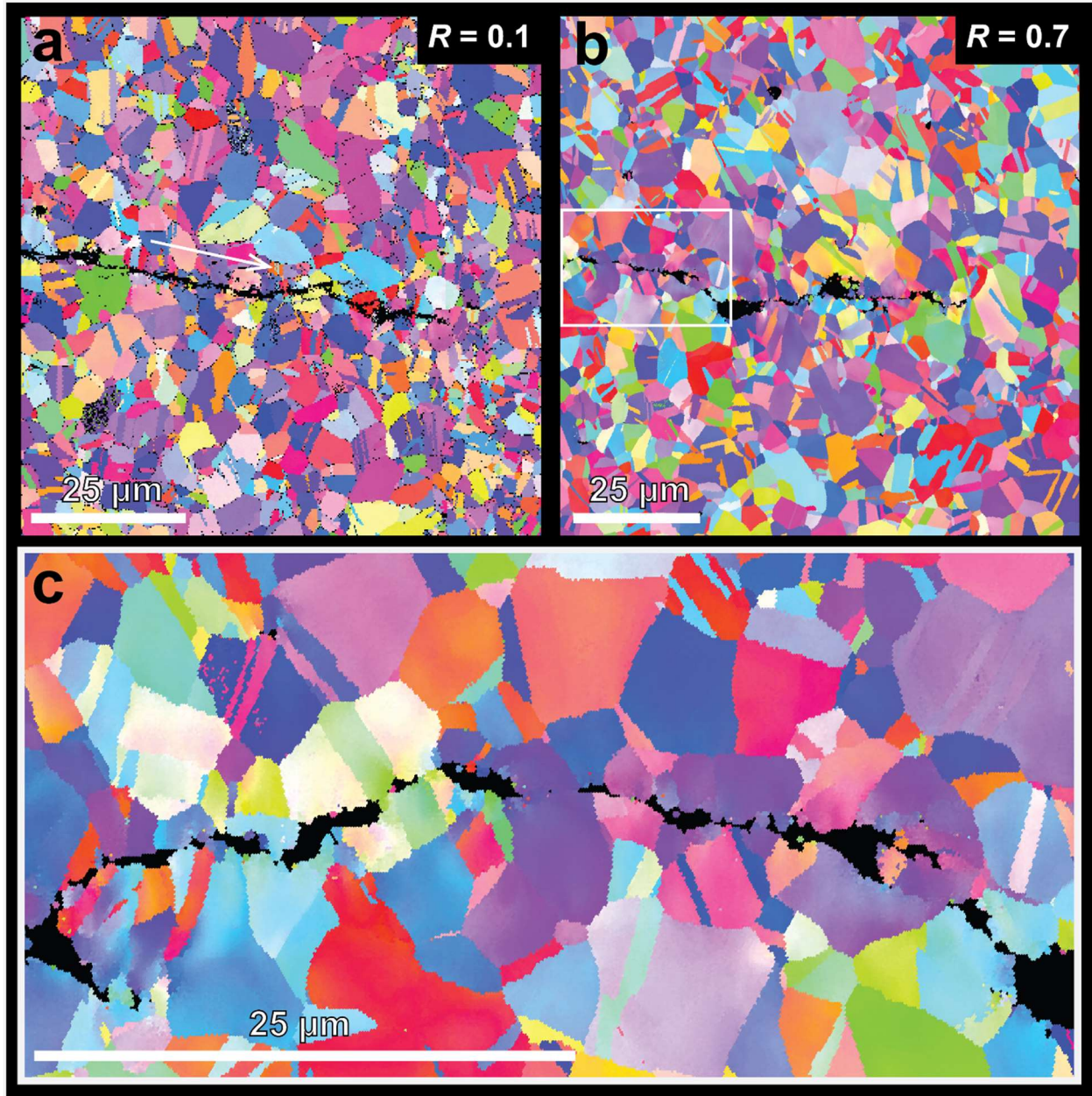
Figure 4.4: EBSD imaging of the crack path in the high stress intensity regions of LN2 tested samples. To examine the potential role of nano-twinning in the shift of the fatigue curve in cryogenically-tested CrMnFeCoNi, detailed EBSD scans were taken at the crack-tip region, the area at which the largest stress intensities were experienced. Images (a) and (b) correspond to imaging of samples subjected to R = 0.1 with $\Delta K \approx 29$ MPa$\sqrt{}$m and R = 0.7 with $\Delta K \approx 20$ MPa$\sqrt{}$m respectively with crack propagation direction indicated by inset arrow. Image (c) shows a higher resolution portion of the crack path of the R = 0.7 sample as indicated by the inset highlight box.

4.4. FRACTOGRAPHY

As can be expected from the BSE images and EBSD scans shown in **Fig. 4.2**, SEM characterization of the fracture surfaces of samples fatigued at 293 K and $R = 0.1$ revealed mainly transgranular crack propagation (**Fig. 4.5 a-c**) with some minor intergranular failure regions (inset of **Fig. 4.5 c**). Most of the transgranular failure region is covered with highly serrated fracture surface features at both the threshold (**Fig. 4.5 a**) and at higher growth rates (**Fig. 4.5 b,c**). The serrations on the fracture surfaces are clearly different in size and shape than typical striations which were found at higher growth rates, as described below; they have far sharper edges (insets **Fig. 4.5 a-c**) and appear to form at specific angles with respect to each other (insets **Fig.4 a,c**). Given that at room temperature, nanoscale deformation twinning has not been found as dominant deformation mechanism in this alloy in both strength and fracture toughness tests [8,10], the latter having significantly higher distributions of crack-tip stresses than those generated during fatigue-crack growth, these periodic serrations cannot be attributed to twinning as the prominent deformation mechanism occurring at the crack tip. Instead, they can only be associated with cyclic slip steps resulting from dislocation motion by planar slip which has been confirmed as the main deformation mechanism for the material at this temperature [10].

Similar to the fracture morphology at 293 K, the fracture surface in the near-threshold region of $R = 0.1$ samples tested at 198 K, at $\Delta K = 6.3$ MPa√m, is highly serrated with sharp edges that form at specific angles, as shown in **Fig. 4.5 d**, indicating that planar slip is also a major deformation mechanism at this temperature. Crack propagation at higher growth rates occurred mainly through intergranular failure, as shown in **Fig. 4.5 e,f** and the inset of Fig. **4.5 f**, consistent with the BSE images and EBSD scans shown in **Fig. 4.3**. Interestingly, polyhedral features can be found on numerous grain boundaries, as indicated by the white arrow in **Fig. 4.5 d** and the insets of **Fig. 4.5e**; we believe that these features are the ends of deformation twins formed perpendicular to the grain boundaries into the grains neighboring the crack front. The increased occurrence of these features at 198 K is consistent with the higher strength of the alloy at these lower temperatures as it is known that deformation twinning in this alloy is a stress-controlled phenomenon [46]. In addition, the serrated straight lines on the grain boundaries appear to be twins that have formed parallel to these grain boundaries rather than perpendicularly to them thereby indicating that twinning at the lower temperature seems to occur more readily than it does at room temperature. This mechanism is consistent with the differences in both the fatigue threshold and the growth rates in the near-threshold regime between 293 K and 198 K.
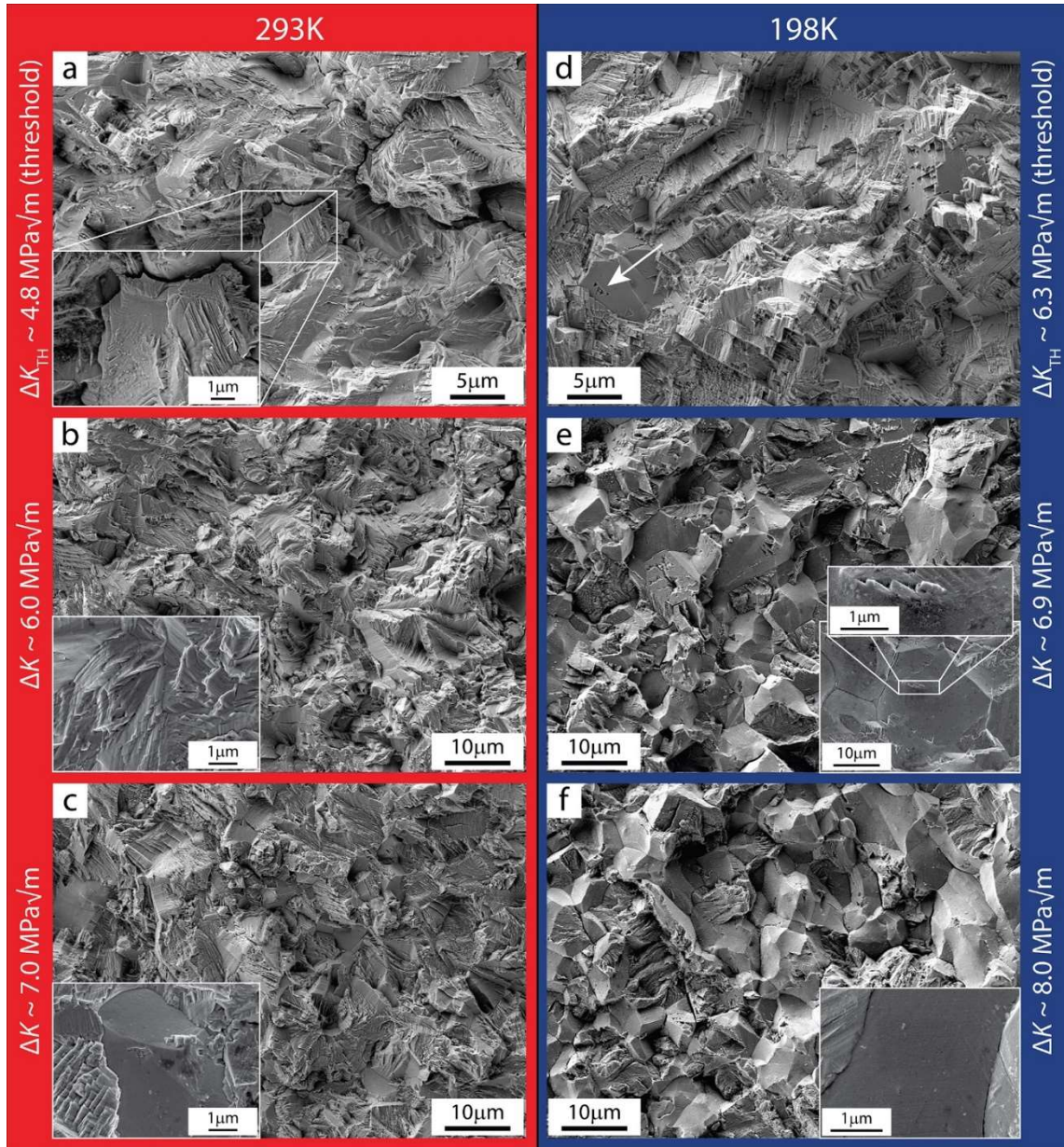
Figure 4.5: Fractographic analysis of CrMnFeCoNi samples tested at *R* = 0.1 in the 293 K and 198 K temperature regimes. Fracture surface characterization of samples tested at 293 K show mainly intergranular crack propagation (a-c) with some minor transgranular failure regions (inset of (c)). The highly serrated fracture surface features covering most of the intergranular failure region (insets of (b) and (c) are likely associated with cyclic slip steps resulting from dislocation motion by planar slip [10]. Similarly, the near-threshold region at 198 K (d) shows planar slip as major deformation mechanism at this temperature whereas at higher growth rates (e,f) crack propagation occurs mainly through intergranular fracture. The white arrow in (d) and the insets of (e) indicate polyhedral features that likely show the ends of deformation twins formed perpendicular to the grain boundaries into the grains neighboring the crack front.

In general, the same trends were largely observed to continue even with testing at higher values of R. Regions of the samples tested at higher ΔK tended to display rougher surface features with prominently displaced striations, a result of the increasing plasticity with increasing stress intensity range applied to the surface. Regions of the samples that were subject to lower values of ΔK, by contrast, tended to show a greater prominence of facet-like features likely characteristic of intergranular fracture. One example of this behavior at higher R may be viewed in **Fig. 4.6**, which depicts the fracture surface of a sample tested at 198 K at R= 0.4 in at both moderate $\Delta K \sim 9$ MPa√m and a higher $\Delta K \sim 17$ MPa√m. Note both images are taken at or beyond the higher end of the range shown in **Fig. 4.5**.
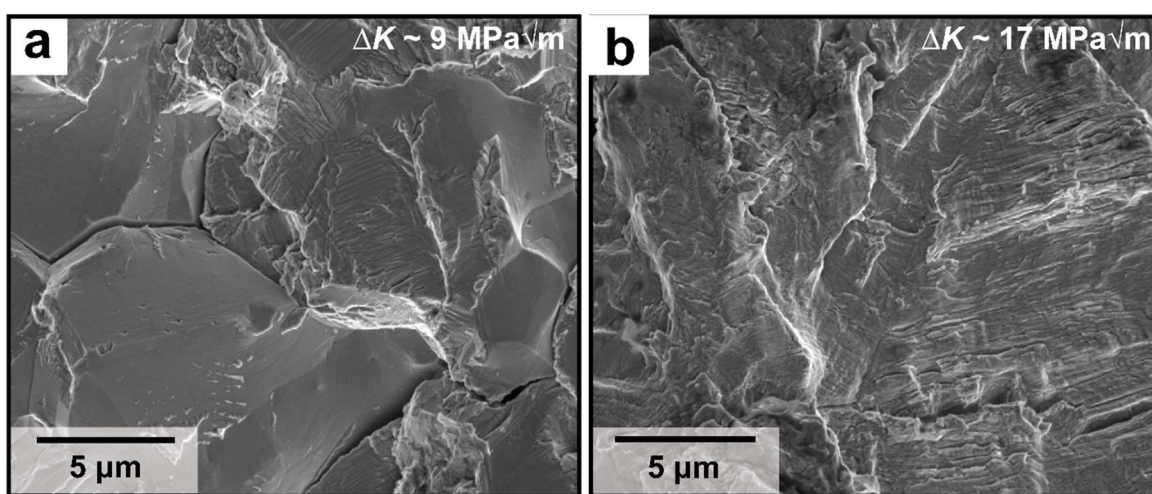
Figure 4.6: Fractographic analysis of CrMnFeCoNi samples tested at $R = 0.4$ at 198 K at two regions subject to different stress intensity ranges. (a) depicts a region subject to moderately high $\Delta K \sim 9$ MPa√m while (b) shows a region subject to high $\Delta K \sim 17$ MPa√m.

Direct comparison between fracture surfaces as a function of R-ratio was also attempted between all nine testing conditions, as displayed in **Fig. 4.7**. This figure portrays regions of each sample type subject to a stress intensity range of approximately $\Delta K \sim 12$ MPa√m; as such, the predicted crack growth rate depicted varied as per **Fig. 3.4**. Unfortunately, due to a degree of post-testing surface oxidation from thermal cycling, fractography of the three LN$_2$ samples proved inconclusive; this oxidation likely occurred due to the condensation of water vapor on the surfaces as samples were removed from the non-reactive nitrogen atmosphere prior to rewarming to ambient temperature. Images from samples tested at 198 K and 293 K indicate a general trend towards increased surface roughness and striation prominence as R-ratio increases. This phenomenon may be in part due to the increased CTOD observed with higher R-ratio: due to the increased opening of the crack tip (and accompanying decrease and elimination of crack closure), fracture surfaces of samples tested at high R-ratio are not subject to the same degree of

wear from the cyclic closing and opening of the fracture surfaces that those testing at lower R may undergo and thus would tend to show sharper features. In general, the fracture surfaces continue the trends previously observed in samples tested at $R= 0.1$, with a transition from rougher, more transgranular fracture behavior to smoother, angular, and more faceting intergranular behavior with decreasing temperature and decreasing R.
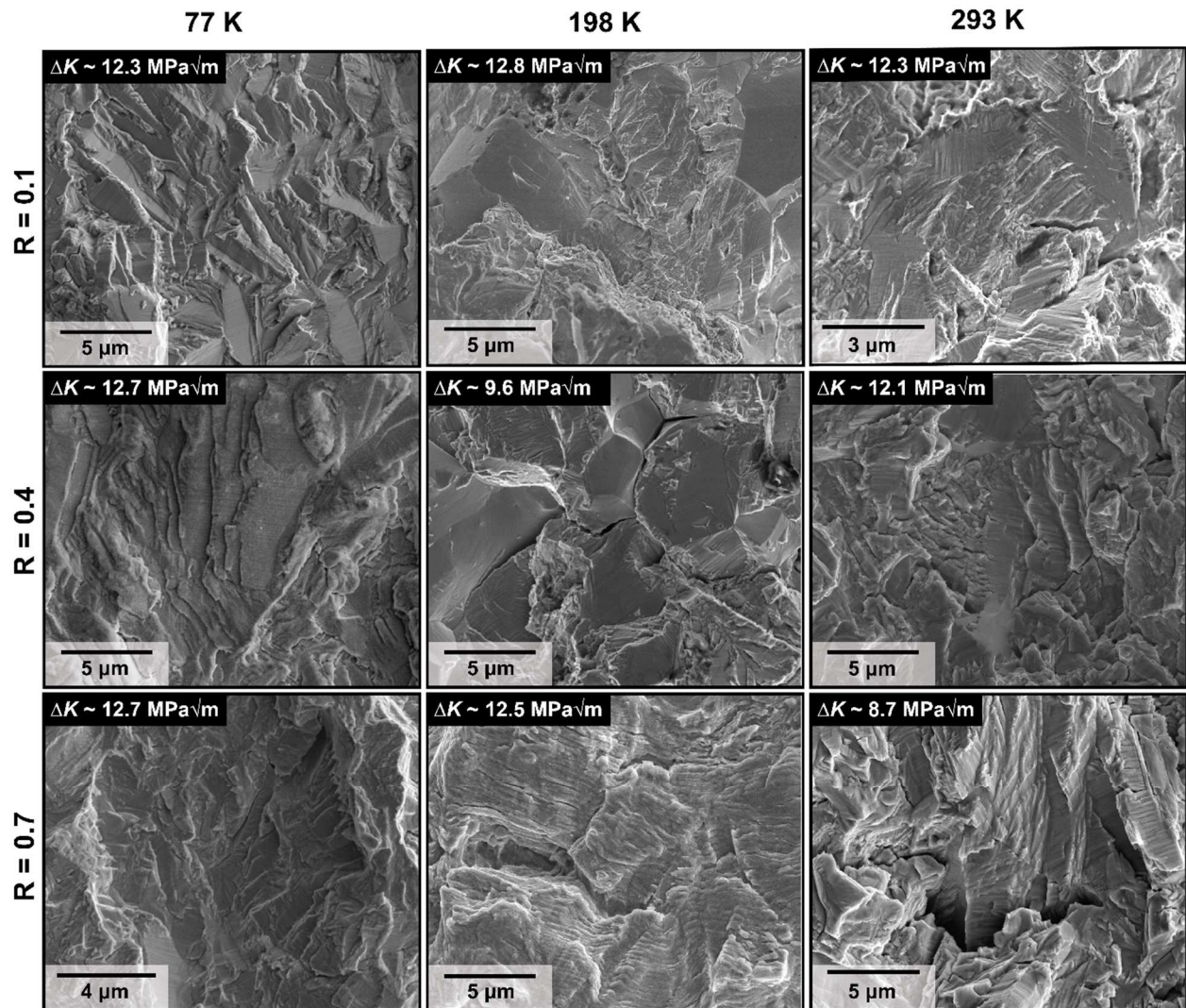
Figure 4.7: Overview of fractography over all nine testing conditions at a moderately high $\Delta K \sim 12$ MPa√m. Images of fracture surfaces at 77 K (left column) show evidence of post-testing oxidation though the general underlying shapes correlate well with the trends observed between 198 K and 293 K tested samples. Higher R seemed to correlate with increased surface plasticity and sharpness of features, as predicted. Additionally, a greater degree of flatter, facet-like features with lower temperature continued to be observed at this higher ΔK though not to the same degree at in **Fig. 4.5**, as expected by the observed increasing degree of transgranular fracture behavior with higher ΔK.

4.4. SUMMARY

Overall, the mechanistic studies performed lend great credence to the hypothesis that the dominant mechanism involved in the shift of the fatigue threshold in the Cantor alloy is that of crack-closure, specifically roughness-induced crack closure. These conclusions are supported by the observations of each section outlined above. Schmidt and Paris analysis allowed an initial, more qualitative check for the potential presence of crack closure, while the quantitative crack closure studies found definitive evidence of crack closure and its different impact at different temperatures. Crack closure could only be measured in samples tested in ambient conditions in samples tested at low R-Ratio, ($R =$ 0.1), while it could be observed in samples tested at cryogenic 198 K for an expanded range of R-ratio, up to $R = 0.4$.

BSE, SE, and EBSD studies of the crack path and fracture surfaces provide visual support to these numeric calculations. Little evidence of deformation twinning, a potential competing mechanism, was observed along the crack path until the imposition of very high stress intensities at very low temperatures (77 K), while some evidence of potential crack closure was observed. Additionally, both crack path studies and fractography indicated a transition from rougher, transgranular fracture to smoother, more intergranular character with the lowering of temperature and R; these surfaces would allow for the 'rezipping' effect of crack closure more readily than the more plastically warped surfaces. Indeed, the smoother surfaces at lower R may also indicate the occurrence of crack closure in and of themselves, as repeated contact of the two surfaces may lead to a wearing effect, thus causing a smoothening of surface features. Thus, I conclude crack closure plays an important if not dominant role in the temperature and R-ratio dependent fatigue behavior of the Cantor alloy.

Chapter 5
Discussion

5.1. COMPARISON TO OTHER ALLOY SYSTEMS

Based on the previously reported mechanical properties of the CrMnFeCoNi alloys in combination with its fatigue performance shown here, the alloy demonstrates high potential as a structural material for engineering applications, especially at lower temperatures [8].

Compared to other HEAs, austenitic stainless steels and twinning-induced plasticity (TWIP) steels, all tested at 298 K at similar testing conditions and comparable in terms of microstructure, the Cantor alloy shows excellent fatigue crack-growth performance at both 298 K and 198 K, as shown in **Fig. 5.1**; details about the individual materials and testing conditions can be found in Table 5.1. The fatigue-crack growth behavior of the CrMnFeCoNi alloy bore the most similarity to that of TWIP steels [61,62]. Akin to our material, TWIP steels also have displayed a lack of twinning behavior under fatigue conditions at room temperature [61,62]. However, they are also known for their high strength complemented with large ductility attributed to their propensity towards deformation twinning at lower temperatures [66]. As shown in **Fig. 5.1**, both their fatigue thresholds and their Paris slopes are comparable to our materials. Furthermore, the CrMnFeCoNi alloy compares favorably in terms of its fatigue threshold to several widely used high-strength steels of both low and moderate carbon content with comparable strength although crack-growth rates in the Paris regime are invariably fairly similar [63-65].

In contrast, the Cantor alloy displayed a lower fatigue threshold to the related Al-containing HEAs [35], but the reason for the disparity may be due to the differences in microstructure between the alloys, particularly between the as-cast structure of the Al-based HEAs and the uniformity of our ~7 μm grain size CrMnFeCoNi, rather than due to inherent compositional differences. As-cast structures have been found to exhibit higher fatigue thresholds than their more finely grained counterparts, which is linked to an increased fracture surface roughness [67]. Moreover, the initially published fatigue data [35] on the Al-CrFeNi-based HEAs may be in error, in terms of unacceptably high fatigue threshold values above 20 MPa√m, due to the small size of the specimens tested and the correspondingly excess plasticity throughout their cross-section. Data on these Al-

containing HEA using larger specimen size, in comparison to the extent of local plasticity, should resolve this issue.
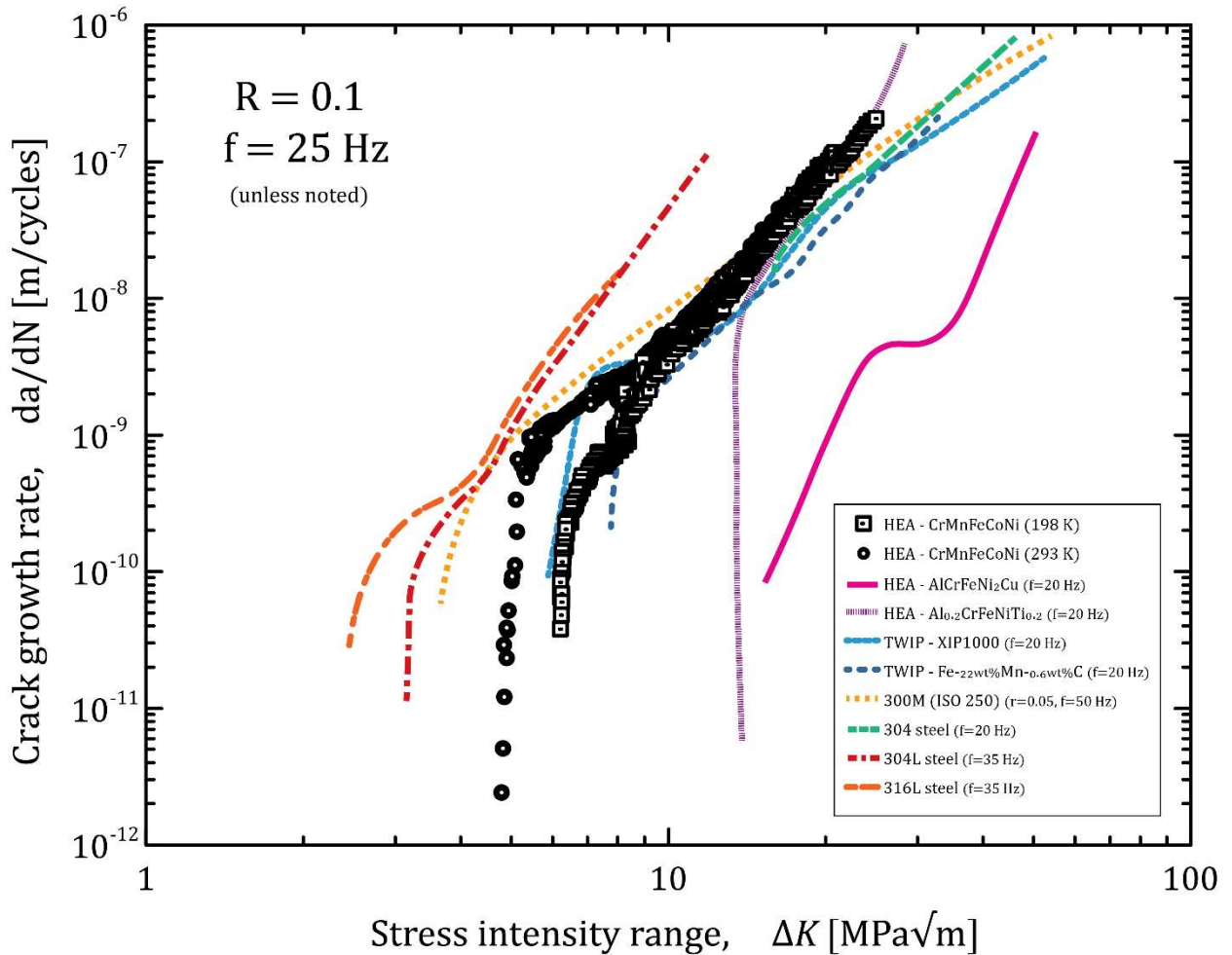
Figure 5.1: Comparison of the fatigue-crack growth behavior of the CrMnFeCoNi high-entropy alloy with austenitic stainless steels and TWIP steels (at 293 K unless otherwise noted). The Cantor alloy displays fatigue behavior most similar to twinning-induced plasticity (TWIP) steels [61-65]. Austenitic stainless steels with comparable microstructure show slightly lower threshold with similar Paris slopes of approximately 3.5-4.5. The Al-containing HEAs demonstrated both higher Paris-regime slopes and fatigue thresholds [35], which may be attributed largely to the as-cast microstructure in combination with the small sample sizes that were used during testing.

Table 5.1: Comparison of fatigue crack growth testing parameters and results for data shown in Fig. 5.1

Alloy	R	Frequency [Hz]	Grain Size [μm]	E [GPa]	Paris slope (m)	Threshold [MPa √m]
HEA – CrMnFeCoNi (293 K)	0.1	25	7	202	3.5	4.8
HEA – CrMnFeCoNi (198 K)	0.1	25	7	210	4.5	6.3
HEA – $AlCrFeNi_2Cu$ [35]	0.1	20	as-cast	-	3.4	17
HEA – $Al_{0.2}CrFeNiTi_{0.2}$ [35]	0.1	20	as-cast	-	4.9	16
XIP 1000-TWIP steel [61]	0.1	20	2	188	2.7	5.9
Fe-22wt%Mn-0.6wt%C TWIP steel [62]	0.1	20	5	-	3.8	7.6
300-M steel (ISO250) [63]	0.05	50	20	205	2.5	3.6
304 steel [64]	0.1	20	-	200	3.8	15.8
304L steel [65]	0.1	35	40	193	5.8	4.8
316L steel [65]	0.1	35	38	193	4.9	3.3

(-) indicates information that was not reported in the literature

5.2. FUTURE WORK

The paucity of information in the literature on the fatigue behavior of HEAs and other metallic systems provides ample opportunity for further experimental and theoretical work to measure, predict, and understand the mechanistic variables at play. This information in turn can be used not only to allow the use of a particular alloy system such as the Cantor alloy with a high degree in confidence for performance expectations but to also aid in the design of future alloy compositions.

With regards to work on understanding the fatigue behavior of the Cantor alloy, several avenues of experimentation present themselves. One of the most promising is an investigation into the fatigue behavior of the 'medium entropy' relative CrCoNi; this alloy has been found to display similar or superior mechanical behavior, particularly strength and fracture toughness, a similar temperature-dependence of said mechanical properties, and a high propensity for deformation twinning. Another avenue of potential future work is to expand the variety of testing conditions the Cantor alloy is subject to including broader temperature range, both into the high temperature regime and potentially even lower than 77 K (liquid He). Other test parameters could be varied as well, such as a greater sampling of R-ratios to more fully characterize Schmidt and Paris behavior of the Cantor alloy or larger sample size to allow testing into the higher, non-linear region of the *da/dN* curve. Further, other environments could be simulated, such as high salinity, to evaluate the performance of this material under harsher conditions in which corrosion or oxidation may affect performance.

Beyond compositional changes and testing conditions, other variants of this alloy could be probed, with the most interesting potentially being varied grain size. The alloy studied here displayed a rather fine and even microstructure, with average grain size <10 μm. The coarsening of the microstructure would likely further effect the fatigue behavior of this system and may be a contributing factor to the large performance difference between this alloy and that of others reported in the literature.

Chapter 6
Conclusions

Just as its strength and toughness have been shown to improve with lowered temperature, the fatigue behavior of the Cantor alloy was also found to display a certain degree of temperature-dependent enhancement, revealing a greater resistance to crack-propagation as temperature was lowered into the cryogenic regime. However, the primary mechanism at work was found to differ from those responsible for the improvement of its other low-temperature mechanical properties. While deformation twinning has been theorized to play a role in the superior fracture toughness the Cantor alloy displays at 77 K, little evidence for deformation twinning was observed in this material. Deformation twinning was only observed at high ΔK and very low temperature (77 K) and was only present in a small fraction of grains in proximity to the grain boundary. As such, this mechanism does not likely play a role in the shifts of fatigue threshold with temperature. Rather, strong evidence was found to indicate roughness-induced crack closure serves as the dominant underlying mechanism of the observed fatigue behavior shifts. This work additionally provides a solid foundation upon which future studies may build, including but not limited to further mechanistic studies of the role and activation of twinning under cyclic loading conditions, investigation of the Cantor alloy's fatigue performance under other environmental conditions, and evaluation of the fatigue behavior of related alloys such as the 'medium entropy' CrCoNi.

In general, the Cantor alloy was found to demonstrate fatigue behavior comparable or superior to other low temperature steel systems including austenic stainless steels and TWIP steels under similar testing conditions. The dearth of fatigue data of HEAs prevents much intra-family comparison, and the little data that is present in the literature describes systems of radically different composition or microstructure. Despite the increasing interest in the HEA family, fatigue studies of these materials remain underrepresented in the literature. As such, this study provides an important step towards closing the gap between scientific research and practical application through the characterization of the fatigue crack-propagation behavior displayed by one of the most prominent and well-researched members of the HEA family.

References

[1] B. Cantor, I. T. H. Chang, P. Knight, A. J. B. Vincent, Microstructural development in equiatomic multicomponent alloys, Mater. Sci. Eng. A 375-377 (2004) 213-218.

[2] J. W. Yeh *et al*, Nanostructured high-entropy alloys with multiple principle elements: novel alloy design concepts and outcomes, Adv. Eng. Mater. 6 (2004) 299-303.

[3] J. W. Yeh, Alloy design strategies and future trends in high-entropy alloys, JOM - J. Min. Met. Mat. S. 65 (12) (2013) 1759-1771.

[4] F. Otto, Y. Yang, H. Bei, E. P. George, Relative effects of enthalpy and entropy on the phase stability of equatomic high-entropy alloys, Acta Mater. 61 (7) (2013) 2628-263.

[5] E. J. Pickering, N. G. Jones, High-entropy alloys: a critical assessment of their founding principles and future prospects, Int. Mater. Rev. 61 (2016) 1743-2804.

[6] P. Chen *et al*, Fatigue behavior of high-entropy alloys: A review, Sci. China Technol. Sci. 61 (2) (2018) 168-178.

[7] B. Gludovatz, E. P. George, R. O. Ritchie, Processing, microstructure and mechanical properties of the CrMnFeCoNi high-entropy alloy, JOM - J. Min. Met. Mat. S. 67 (2016) 2262-2270.

[8] B. Gludovatz *et al*, A fracture-resistant high-entropy alloy for cryogenic applications, Science 345 (2014) 1153-1158.

[9] M. J. Yao, K. G. Pradeep, C. C. Tasan, D. Raabe, A novel, single phase, non-equiatomic FeMnNiCoCr high-entropy alloy with exceptional phase stability and tensile ductility, Scripta Mater. 72-73 (2014) 5-8.

[10] F. Otto *et al*, The influences of temperature and microstructure on the tensile properties of CoCrFeMnNi high-entropy alloy, Acta Mater. 61 (2013) 5743-5755.

[11] A. Gali, E. P. George, Tensile properties of high-and medium-entropy alloys, Intermetallics 39 (2013) 74-78.

[12] Y. F. Ye, Q. Wang, J. Lu, C. T. Liu, Y. Yang, High-entropy alloy: challenges and prospects, Mater. Today 19(6) (2016) 349-362.

[13] Y. Zhang, X. Yang, P. K. Liaw, Alloy design and properties optimization of high-entropy alloys, JOM - J. Min. Met. Mat. S. 64 (7) (2012) 830-838.

[14] Y. J. Zhou, Y. Zhang, Y. L. Wang, G. L. Chen, Solid solution alloys of AlCoCrFeNiTi$_x$ with excellent room-temperature mechanical properties, Appl. Phys. Lett. 90 (18) (2007) 181904.

[15] S. T. Chen *et al*, Microstructure and properties of age-hardenable Al$_x$CrFe$_{1.5}$MnNi$_{0.5}$ alloys, Mater. Sci. Eng. A 527 (21-22) (2010) 5818-5825.

[16]   C. Y. Hsu, C. C. Juan, W. R. Wang, T. S. Sheu, J. W. Yeh, S. K. Chen, On the superior hot hardness and softening resistance of $AlCoCr_xFeMo_{0.5}Ni$ high-entropy alloys, Mater. Sci. Eng. A 528(10-11) (2011) 3581-3588.

[17]   O. N. Senkov, J. M. Scott, S. V. Senkova, D. B. Miracle, C. F. Woodward, (2011). Microstructure and room temperature properties of a high-entropy TaNbHfZrTi alloy, J. Alloys Compd. 509 (20) (2011) 6043-6048.

[18]   C. J. Tong *et al*, Mechanical performance of the $Al_xCoCrCuFeNi$ high-entropy alloy system with multiprincipal elements, Metall. Mater. Trans. A 36 (5) (2005) 1263-1271.

[19]   C. Y. Hsu, J. W. Yeh, S. K. Chen, T. T. Shun, Wear resistance and high-temperature compression strength of Fcc $CuCoNiCrAl_{0.5}Fe$ alloy with boron addition, Metall. Mater. Trans. A 35 (5) (2004) 1465-1469.

[20]   M. H. Chuang, M. H. Tsai, W. R. Wang, S. J. Lin, J. W. Yeh, Microstructure and wear behavior of $Al_xCo_{1.5}CrFeNi_{1.5}Ti_y$ high-entropy alloys, Acta Mater. 59 (16) (2011) 6308-6317.

[21]   M. H. Chuang *et al*, Intrinsic surface hardening and precipitation kinetics of $Al_{0.3}CrFe_{1.5}MnNi_{0.5}$ multi-component alloy, J. Alloys Compd. 551 (2013) 12-18.

[22]   M. H. Tsai *et al*, Thermal stability and performance of NbSiTaTiZr high-entropy alloy barrier for copper metallization, J. Electrochem. Soc. 158 (11) (2011) H1161-H1165.

[23]   Y. Zhang *et al*, Microstructures and properties of high-entropy alloys, Prog. Mater. Sci. 61 (2014) 1-93.

[24]   R. V. Marrey, R. Burgermeister, R. B. Grishaber, R. O. Ritchie, Fatigue and life prediction for cobalt-chromium stents: a fracture mechanics analysis, Biomaterials 27 (9) (2006) 1988-2000.

[25]   K. Alagarsamy *et al*, Mechanical Properties of High Entropy Alloy $Al_{0.1}CoCrFeNi$ for Peripheral Vascular Stent Application, Cardiovasc. Eng Technol. 7 (4) (2016) 448-454.

[26]   A. Runciman, D. Xu, A. R. Pelton, R. O. Ritchie, An equivalent strain/Coffin–Manson approach to multiaxial fatigue and life prediction in superelastic Nitinol medical devices, Biomaterials 32 (22) (2011) 4987-4993.

[27]   J. N. Yang, S. Chen, Fatigue reliability of gas turbine engine components under scheduled inspection maintenance, J. Aircraft 22 (1985) 415-422.

[28]   B. A. Cowles, High cycle fatigue in aircraft gas turbines—an industry perspective, Int. J. Fracture 80 (2-3) (1996) 147-163.

[29]   Y. Zhang *et al*, Microstructures and properties of high-entropy alloys, Prog. Mater. Sci. 61 (2014) 1-93.

[30]   M. C. Gao, J. W. Yeh, P. K. Liaw, Y. Zhang, High-Entropy Alloys, Springer International Publishing (2016).

[31]   M. A. Hemphill *et al*, Fatigue behavior of Al0.5CoCrCuFeNi high entropy alloys, Acta Mater. 60 (2012) 5723-5734.

[32]   M. A. Hemphill, Fatigue behavior of high-entropy alloys, Master's thesis (2012).

[33]   Z. Tang, T. Yuan, C.-W. Tsai, J. W. Yeh, C. D. Lundin, P. K. Liaw, Fatigue behavior of a wrought Al$_{0.5}$CoCrCuFeNi two-phase high-entropy alloy, Acta Mater. 99 (2015) 247-258.

[34]   K. Liu *et al*, (2019), Fatigue behavior of ultrafine grained triplex Al$_{0.3}$CoCrFeNi high entropy alloy, Int. J. Fatigue 158 (2019) 116-120.

[35]   M. Seifi *et al*, Fracture toughness and fatigue crack growth behavior of as-cast high-entropy alloys, JOM - J. Min. Met. Mat. S. 67 (2015) 2288-2295.

[36]   N. Stepanov *et al*, Effect of cryo-deformation on structure and properties of CoCrFeNiMn high-entropy alloy, Intermetallics 55 (2015) 8-17.

[37]   F. Otto *et al*, Decomposition of the single-phase high-entropy alloy CrMnFeCoNi after prolonged anneals at intermediate temperatures, Acta Mater. 112 (2016) 40-52.

[38]   C. C. Tasan, Y. Deng, K. G. Pradeep, M. J. Yao, H. Springer, D. Raabe, Composition dependence of phase stability, deformation mechanisms, and mechanical properties of the CoCrFeMnNi high-entropy alloy system, JOM - J. Min. Met. Mat. S. 66 (2014) 1993-2001.

[39]   N. G. Jones, J. W. Aveson, A. Bhowmik, B. D. Conduit, H. J. Stone, On the entropic stabilization of an Al$_{0.5}$CrFeCoNiCu high entropy alloy, Intermetallics 54 (2014) 148-153.

[40]   D. Ma, B. Grabowski, F. Körmann, J. Neugebauer, D. Raabe, Ab initio thermodynamics of the CoCrFeMnNi high entropy alloy: importance of entropy contributions beyond the configurational one, Acta Mater. 100 (2015) 90-97.

[41]   J. W. Yeh, Physical metallurgy of high-entropy alloys, JOM - J. Min. Met. Mat. S. 67 (2015) 2254-2261.

[42]   D. B. Miracle, J. D. Miller, O. N. Senkov, C. Woodward, M. D. Uchic, J. Tiley, Exploration and development of high entropy alloys for structural applications, Entropy 16 (2014) 494-525.

[43]   B. Cantor, Multicomponent and high entropy alloys, Entropy 16 (2014) 4749-4768.

[44]   R. O. Ritchie, The conflicts between strength and toughness, Nat. Mater. 11 (2011) 817-822.

[45]   Y. Zang *et al*, Microstructures and properties of high-entropy alloys, Prog. Mater. Sci. 61 (2014) 1-93.

[46]   G. Laplanche, O. Horst, F. Otto, G. Eggeler, E. P. George, Microstructural evolution of a CoCrFeMnNi high-entropy alloy after swaging and annealing, J. Alloys Compd. 647 (2015) 548-57.

[47] ASTM Standard E1820, Standard test method for measurement of fracture toughness, ASTM International, West Conshohocken, PA (2014). www.astm.org.

[48] C. J. Gilbert, J. M. McNaney, R. H. Dauskardt, R. O. Ritchie, Back-face strain compliance and electrical-potential crack length calibrations for the disk-shaped compact-tension DC(T) specimen, JTEVA 22 (1994) 117-120.

[49] B. Gludovatz, S. E. Naleway, R. O. Ritchie, J. J. Kruzic, Size-dependent fracture toughness of bulk metallic glasses, Acta Mater. 70 (2014) 198-207.

[50] K. Heckel, R. Wagner, The tensile fatigue behavior of CT-specimens with small notch root radius, Int. J. Fatigue 11 (1) (1975) 135-140.

[51] ASTM Standard E647, Standard test method for measurement of fatigue crack growth rates, ASTM International, West Conshohocken, PA (2013). www.astm.org.

[52] R. Pippan, K. Haberz, H. P. Stüwe, The plastic deformation of fracture surface contacts in fatigue, Eng. Fract. Mech. 53(3) (1996) 441-448.

[53] G. Laplanche, P. Gaduad, O. Horst, F. Otto, G. Eggeler, E. P. George, Temperature dependencies of the elastic moduli and thermal expansion coefficient of an equiatomic, single phase CoCrFeMnNi high-entropy alloy, J. Alloy Compd. 623 (2015) 348-53.

[54] A. Haglund, M. Koehler, D. Catoor, E. P. George, V. Keppens, Polycrystalline elastic moduli of a high-entropy alloy at cryogenic temperatures, Intermetallics 58 (2015) 62-64.

[55] R. O. Ritchie, W. Yu, Short crack effects in fatigue: a consequence of crack tip shielding, Small Fatigue Cracks, R. O. Ritchie and J. Lankford, eds., TMS-AIME (1986) 167-189.

[56] S. Suresh, R. O. Ritchie, A geometric model for fatigue crack closure induced by fracture surface roughness, Metall. Trans. A 13A (1982) 1627-1631.

[57] R. O. Ritchie, Mechanisms of fatigue crack propagation in metals, ceramics and composites: role of crack tip shielding, Mater. Sci. Engng. 103 (1998) 15-28.

[58] L. Lawson, E. Y. Chen, M. Meshii, Near-threshold fatigue: a review, Int. J. Fatigue 21 (1999) S15-S34.

[59] R. A. Schmdt, P. C. Paris, Theshold for fatigue crack propagation and the effects of load ratio and frequency, ASTM STP 536 (1973) 79-94.

[60] K. T. Venkateswara Rao, W. Yu, R. O. Ritchie, Fatigue crack propagation in aluminum-lithium alloy 2090: part I. long crack behavior, Metall. Trans. A, 19A (3) (1988) 549-561.

[61] T. Niendorf. *et al*, Fatigue crack growth - microstructure relationships in a high-manganese austenitic TWIP steel, Mater. Sci. Eng. A 527 (2010) 2412-2417.

[62]   P. Ma *et al*, Fatigue crack growth behavior of a course- and a fine-grained high manganese austenitic twin-induced plasticity steel, Mater. Sci. Eng. A 605 (2014) 160-166.

[63]   R. O. Ritchie, Near-threshold fatigue crack propagation in ultra-high strength steel: influence of load ratio and cyclic strength, J. Eng. Mater.-T. ASME 99 (1977) 195-204.

[64]   L. W. Tsay, Y. C. Liu, M. C. Young, D. Y. Lin, Fatigue crack growth of AISI 304 stainless steel welds in air and hydrogen, Mater. Sci. Eng. A 374 (2004) 204-210.

[65]   C. Sarrazin-Baudoux, J. Petit, C. Amzallag, Near-threshold fatigue crack propagation in austenitic stainless steel, Paper presented at ECF14, Cracow, 2002.

[66]   J. W. Christian, S. Mahajan, Deformation twinning, Prog. Mater. Sci. 39 (1995) 1-157.

[67]   A.-L. Gloanec, G. Hénaff, D. Bertheau, P. Belaygue, M. Grange, Fatigue crack growth behaviour of a gamma-titanium-aluminide alloy prepared by casting and powder metallurgy, Scr. Mater. 49(9) (2003) 825-830.